nature materials

Article

https://doi.org/10.1038/s41563-023-01488-2

A multiscale ion diffusion framework sheds light on the diffusion–stability–hysteresis nexus in metal halide perovskites

In the format provided by the authors and unedited

Table of Contents

1. SIMS data analysis 3
2. Lack of Surface Diffusion in Lateral Diffusion 6
3. RSF calculation 10
4. Notes on diffusion 14
5. Harrison Classification 15
6. PL Microscopy 18
7. X-ray photoemission spectroscopy 19
8. I^- diffusion in $MAPbBr_3$ single crystal 21
9. Note on PL and Superoxide 24
10. Double-Halide Diffusion 33
11. GB passivation 34
12. Halide exchange 36

List of Figures

Supplementary Fig. S1: Conversion of 3D map to 1D SIMS profile 3
Supplementary Fig. S2: Total ion count profile 4
Supplementary Fig. S3: 2D SIMS map of foreign halide diffusion in different MHPs 5
Supplementary Fig. S4: 1D SIMS map of foreign halide diffusion in different MHPs 6
Supplementary Fig. S5: Possible effects of surface diffusion 8
Supplementary Fig. S6: Depth profilometry of I^- diffusion into $MAPbBr_3$ single crystal 10
Supplementary Fig. S7: TIC normalized Br^- count in $MAPbBr_3$ and $FAPbBr_3$ 11
Supplementary Fig. S8: RSF calculation 12
Supplementary Fig. S9: SIMS profiles reproducibility 13
Supplementary Fig. S10: Quantitative diffusion coefficient extraction 14
Supplementary Fig. S11: Finite versus constant source solution 17
Supplementary Fig. S12: Different annealing time effects on diffusion 17
Supplementary Fig. S13: µPL map of I^- diffusion into $MAPbBr_3$ thin film 18
Supplementary Fig. S14: XPS spectra of reference samples 19
Supplementary Fig. S15: XPS spectra of diffused samples after annealing 20
Supplementary Fig. S16: Lateral distribution of Pb^0 and I 20

Supplementary Fig. S17: XRD and SEM results of overlap region 21
Supplementary Fig. S18: T-dependent of I^- diffusion in $MAPbBr_3$ single crystal 23
Supplementary Fig. S19: I^- background count in single crystal and thin film 24
Supplementary Fig. S20: Superoxide yield comparison 26
Supplementary Fig. S21: Steady state and time resolved PL 27
Supplementary Fig. S22: Photodegradation in dry air 28
Supplementary Fig. S23: MPP tracking 29
Supplementary Fig. S24: SEM of reference samples 30
Supplementary Fig. S25: *J-V* curves and HIs 31
Supplementary Fig. S26: Mixed halide *J-V* curves 32
Supplementary Fig. S27: Double halide diffusion 34
Supplementary Fig. S28: PCBM passivation effects on D_V and D_{GB} 35
Supplementary Fig. S29: PEAI passivation effects on D_V and D_{GB} 35
Supplementary Fig. S30: Effect of the substrate in halide exchange 30
Supplementary Fig. S31: Halide exchange mechanism in polycrystalline MHPs 31
Supplementary Fig. S32: UV-Vis absorption of bilayer samples 32

List of Tables

Supplementary Table S1: Different annealing time effects on diffusion 18
Supplementary Table S2: Photovoltaic characteristics of fresh $MAPbI_3$ PVs 32
Supplementary Table S3: Photovoltaic characteristics of fresh $FA_{0.85}Cs_{0.15}PbI_3$ PVs 32
Supplementary Table S4: Photovoltaic characteristics of fresh mixed halide PVs 33

1. *SIMS data analysis*

All the SIMS measurements were performed in Non-Interlaced mode to minimize the effect of charging during measurements. The Non-Interlaced measurements were performed with an analysis time of 2 seconds, a sputtering time of 10 seconds, and a pause time of 0.5 s. The sputter area and analyzed areas of 400×400 μm^2 and 200×200 μm^2 are used for all thin film samples. A random raster with a 256×256 pixel was used during the data collection. As a result, each measurement provides a depth profile and a 3D map of the lateral geometry of the sample. To increase the signal-to-noise ratio, the sum of the ion counts through the thickness is used to construct a 2D SIMS profile as shown in **Fig. S1a** and **S1b**. Also, to avoid the effect of beam instability during the first few seconds of depth profiling and the surface diffusion the count from the first layer of analysis was excluded from the sum through the thickness. The 2D map was further reduced to a 1D SIMS profile by integration of the count over the axis perpendicular to the diffusion direction (y-axis) as shown in **Fig. S1c**.

To correct for the effect of yield change in a particular SIMS profile each profile is divided by the total count of ions in the same range. For example, the total count, and Br^- count in $MAPbI_3$ sample are plotted in **Fig. S2**. As can be seen, besides the gradient that can be observed in Br^- profile the total count also shows a gradient with a similar shape to Br^- signal. It is worth pointing that, although the shape of the total count is similar to the halide count, the magnitude of this change, from left to right, is much smaller than the change in halide ions count. In the presented case for instance, during the 200 µm analyzed region, the halide count drops by almost 800% while the total count only changes by 20%.

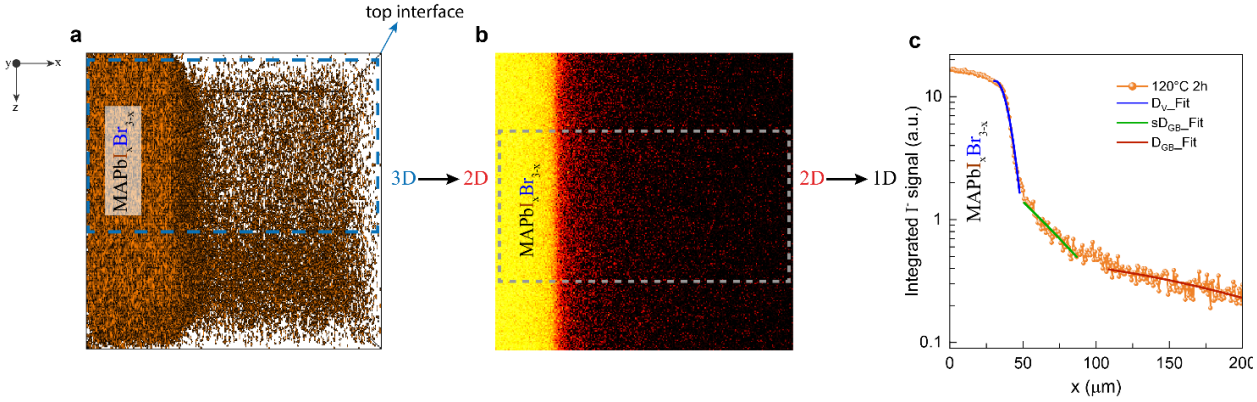

Fig. S1. **a**, an example of 3D SIMS profile showing I^- diffusion into the $MAPbBr_3$ polycrystalline film annealed at 120°C for 2 hours. The z-axis in this case represents the thickness of the film and sputter time. The 3D SIMS map is stretched over z-axis for clarity. The blue box shows the layers which were used to

construct the **b**, 2D SIMS map. The lower part of the 3D region is excluded from the summation to avoid the effect of the bottom interface. **b**, the gray dashed line shows an example of a region, which is used for the integration and construction of 1D SIMS **c**, profile. Depending on the sharpness of the diffusion front different integration region or range is used in different samples.

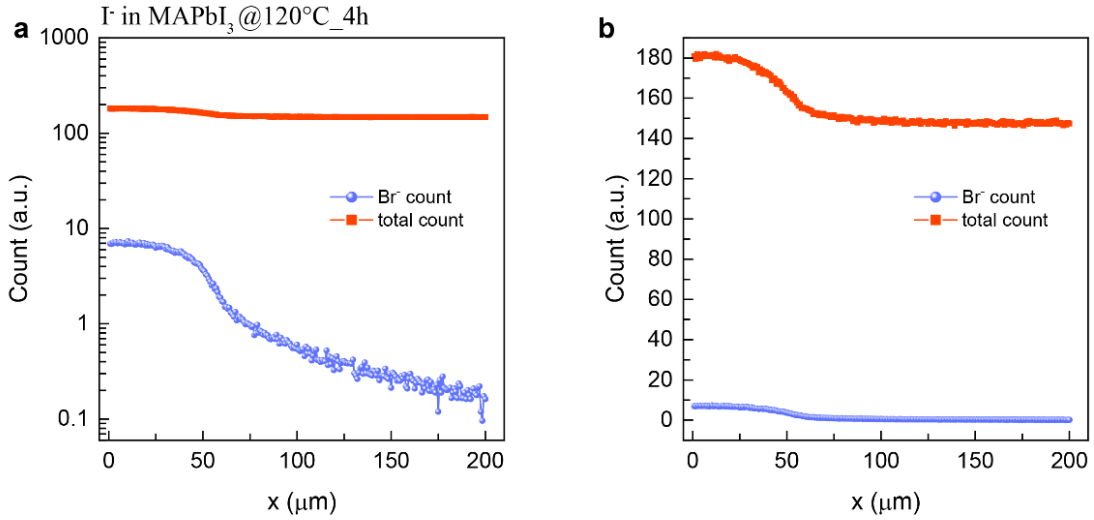

Fig. S2. Plotted total ion count and Br^- count for 1D SIMS profile of Br^- diffusion into the $MAPbI_3$ polycrystalline film annealed at 120°C for 4 hours, **a**, and **b**, in log and linear scale, respectively.

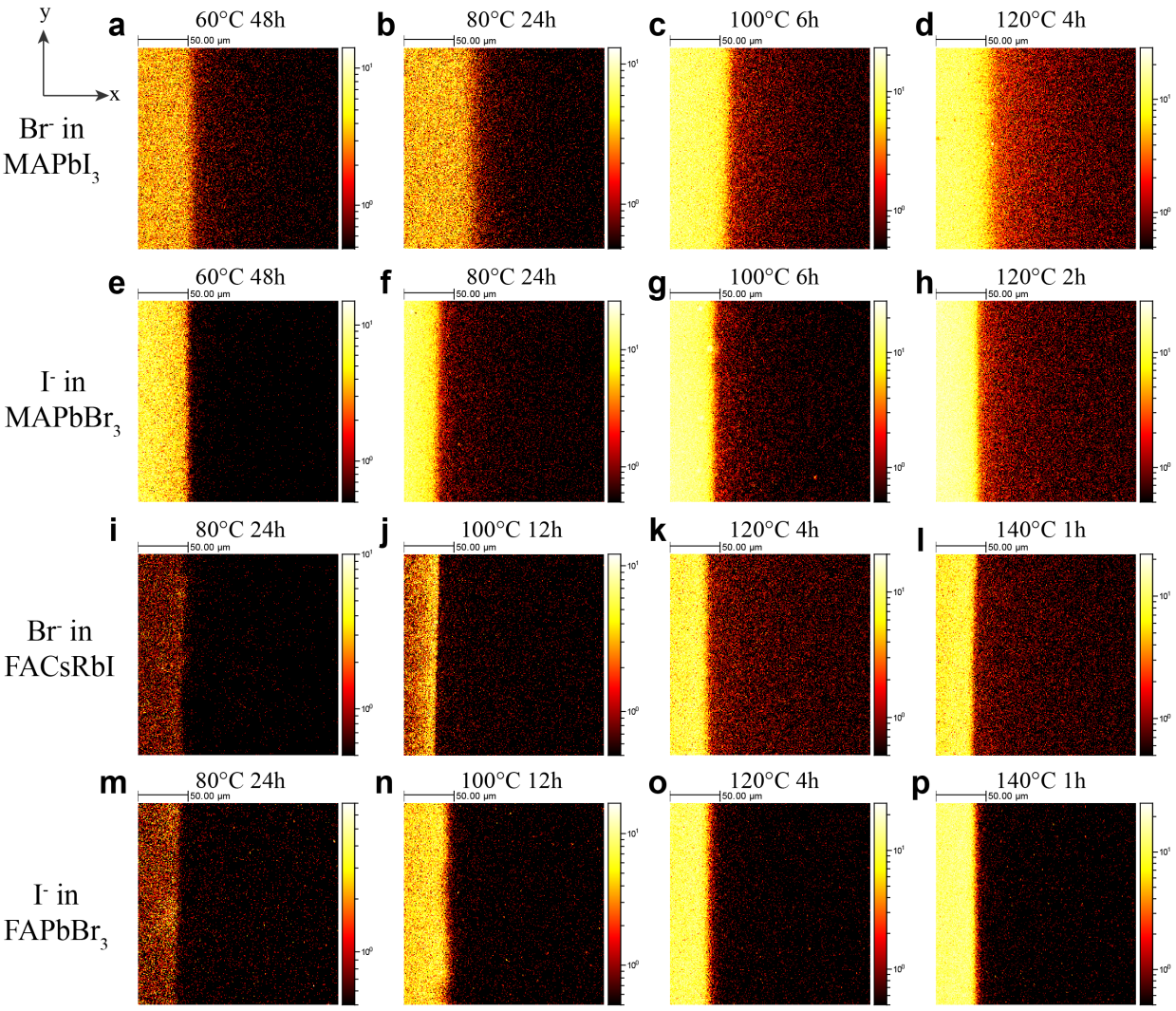

Fig. S3. 2D SIMS map of **a-d**, Br^- diffusion into $MAPbI_3$, **e-h**, I^- diffusion into $MAPbI_3$, **i-l**, Br^- diffusion into FACsRbI, and **m-p**, I^- diffusion into $FAPbBr_3$. The brighter regions in both exchange and lateral parts of the diffusion show the higher intensity of ions. We should emphasize that the count between different MHP systems can not directly be associated with the composition of the foreign halides since these profiles are not corrected by either the total or the reference count and solely represent the un-normalized halide count in each sample. The color bars have the units of counts/pixel.

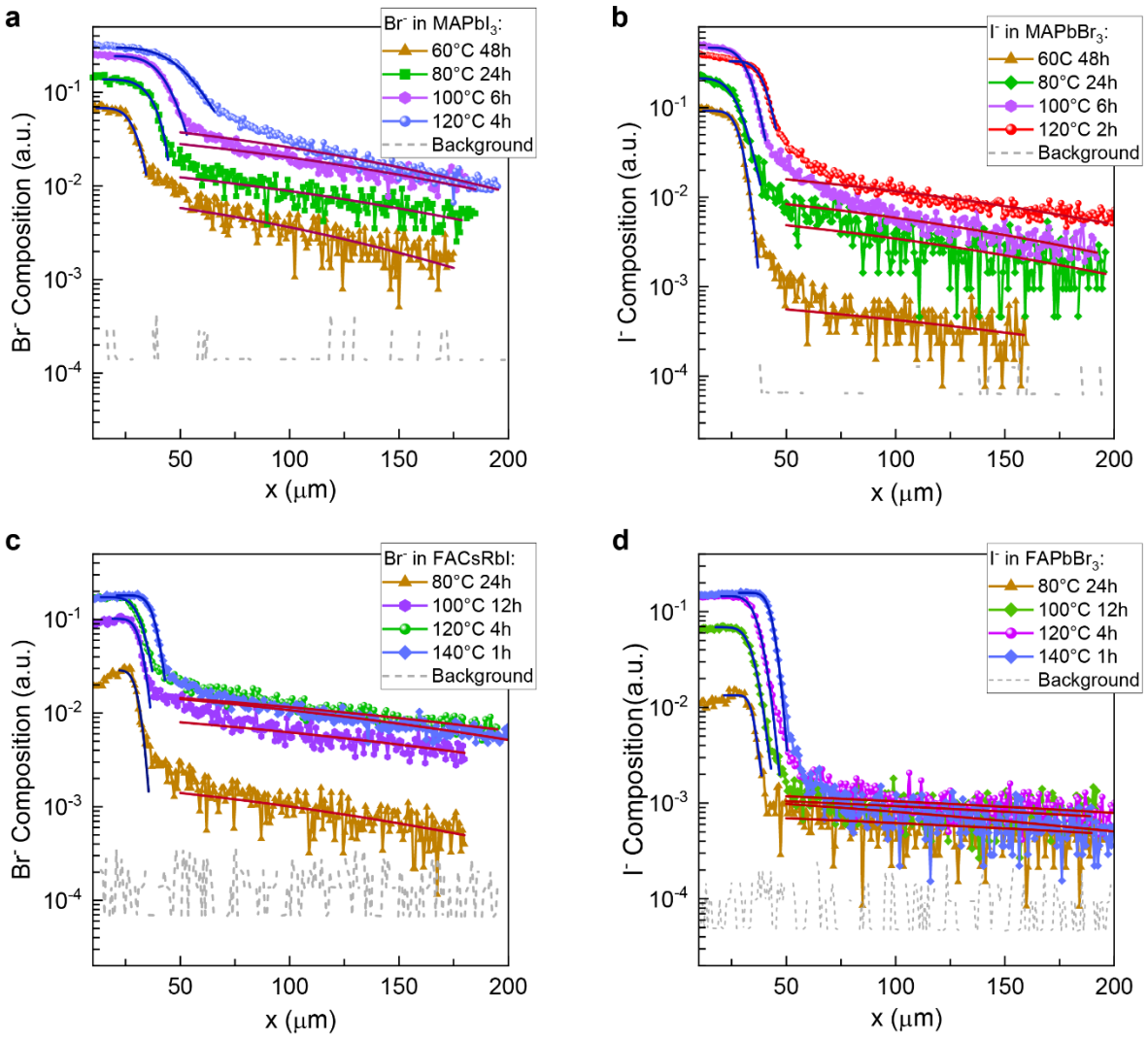

Fig. S4. 1D SIMS profiles of **a**, Br^- diffusion into $MAPbI_3$, **b**, I^- diffusion into $MAPbBr_3$, **c**, Br^- diffusion into FACsRbI, and **d**, I^- diffusion into $FAPbBr_3$. The blue and red lines show the *erfc* fits to volume and GB diffusion, respectively, for D_V and D_{GB} extraction. Due to the presence of x_0 as the source displacement factor and a fitting parameter, the diffusion coefficients extracted from diffusion profiles are insensitive to the lateral position of the profiles. Such lateral shift only affects the x_0. As a result, some of the diffusion profiles are shifted laterally for clarity.

2. Lack of Surface Diffusion in Lateral Diffusion

Surface diffusion in polycrystalline systems has been shown to take place with orders of magnitude faster diffusion rate compared to GB and volume diffusions[1]. As a result, it is important for us to consider the possibility of surface diffusion and the role that these ions can play as a secondary diffusion source. An important consideration regarding the possible effects of surface diffusion in volume and GB diffusion profiles is the limited thickness of the surface layer as a diffusion source compared to the thickness of the perovskite layers (380-410 nm). In a case in which the free surface

acts as a source for volume and GB diffusion, due to the limited concentration of diffusant ions on the free surface (with a maximum ratio of 50 wt% between bromine and iodine[2]), we expect two different forms of gradients to exist in the 1D SIMS profile. First, a surface diffusion source creates a vertical gradient with higher concentrations of foreign/diffusant ions close to the surface. Here we choose two different 3D SIMS profiles which are analogous to other profiles studied in this work (Br^- diffusion in $MAPbI_3$ and FACsRbI). To investigate depth profiles for foreign Br^- ions in the host MHPs we choose five different analyzing areas perpendicular to the diffusion front as shown in **Fig. S5 b** and **g**. The 1D depth profiles representing these selected areas are presented in **Fig. S5 d** and **i**. As can be seen, no apparent depth gradient can be observed in these profiles. It is also worth noting that the slight increase in Br^- count on the top surface and after ~200 s sputtering time is associated with the increase in oxygen ions count which increases the halide ions yield on those regions. The second type of foreign halide gradient that is expected in the case of surface diffusion source would be the gradient in diffusion profiles when collected at different depths as shown in **Fig. S5 c** and **h**. Due to a finite amount of foreign halides on the surface, even after considering the possibility of replenishing ion concentrations on the surface, in the case of the free surface acting as a diffusion source, we expect profiles collected from the stacks closer to the surface show a different diffusion behavior compared to the profiles collected at the stacks closer to the middle of the layer (stack 1 compared to stack 2 in **Fig. S5c**). While, when we compare the diffusion profiles collected from different depths (**Fig. S5e** and **j**) we observe a complete overlap between these profiles. Hence, due to the lack of a gradient through the depth and the complete overlap of the diffusion profiles collected at different depths we can conclude that the possibility of surface diffusion acting as a source and altering the volume and GB diffusion can be ruled out. It is also worth mentioning that although these results rule out the effects of surface diffusion as a source for volume and GB diffusion profiles, they do not rule out the existence of surface diffusion channels in MHPs. Surface diffusion characterization in different MHP compositions requires a more detailed investigation that is outside the scope of this study.

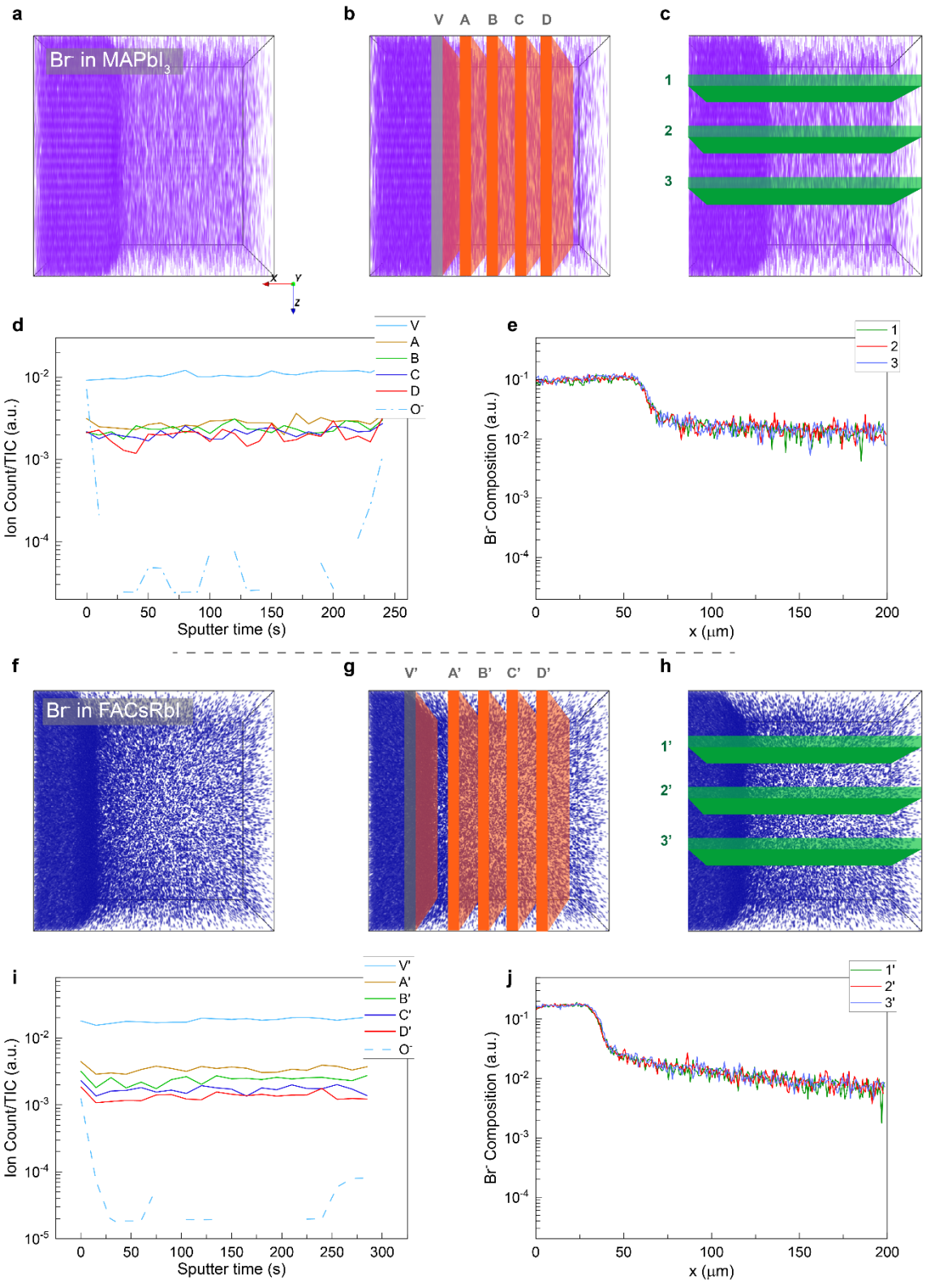
a
Br⁻ in MAPbI3
b
V A B C D
c
1
2
3
d
V
A
B
C
D
O⁻
Ion Count/TIC (a.u.)
Sputter time (s)
e
1
2
3
Br⁻ Composition (a.u.)
x (μm)
f
Br⁻ in FACsRbI
g
V' A' B' C' D'
h
1'
2'
3'
i
V'
A'
B'
C'
D'
O⁻
Ion Count/TIC (a.u.)
Sputter time (s)
j
1'
2'
3'
Br⁻ Composition (a.u.)
x (μm)

Fig. S5. a-c, and **f-h** *x-y* plane view of 3D diffusion profiles of Br^- into PCBM passivated $MAPbI_3$ at 100°C and Br^- into FACsRbI at 120°C. These profiles are chosen due to the higher counts of halides in the GB diffusion regions. The orange vertical stacks show the region of interest (ROI) selected 1D depth profiles. V and V' stacks represent ROIs that are on the interface between volume and GB diffusion regions. The drop in Br^- count from A-D (**d**) and A'-D' (**i**) is due to the gradient caused by the diffusion profile in *-x* orientation. The solid lines in (**d**) and (**i**) show the TIC normalized Br^- signal while the dashed blue lines show the oxygen ions normalized counts. The green lateral stacks show the ROIs for diffusion profiles parallel to the diffusion front. The diffusion profiles from horizontal stacks are shown in **e** and **j**. The 3D images are stretched in *z* orientation for clarity.

We also acquired diffusion profiles for I^- diffusion into $MAPbBr_3$ single crystals. We choose single crystals for this study since MHP thin films with thicknesses over 2 μm are challenging to fabricate and suffer from a nonuniform and porous morphology that could affect both the depth profile and interpretation of the results. That being said in general a long-range depth profilometry of single crystals is also not free of challenges and artifacts. We noticed that although Cs^+ is a good source for sputtering of thin film MHPs with a thickness below 1 μm, for deep sputtering of single crystal $MAPbBr_3$ with a crater depth over 1 μm Cs^+ causes some artifacts and spikes in ion counts. On the other hand, the sputtering of single crystals using a gas cluster ion beam (GCIB) provides a more uniform count (**Fig S6a**). The second challenge of single crystal sputtering is LMIG beam instability during long-term measurements. For instance, the layer by layer data acquisition and sputtering time needed for the data collection of the blue plot in **Fig. S6a** takes over 7 hours. During this period, the instability of the LMIG gun and charging of the samples, examples of which are shown by black arrows in **Fig. S5 a** and **b** interrupt the continuity of the measurements. Subsequently, we extrapolated the diffusion profile acquired using a GCIB gun to estimate diffusion length for I^- diffusion into $MAPbBr_3$ single crystals. By taking 3×10^{-5} as the background count of iodide in pristine $MAPbBr_3$ single crystals we find the diffusion length of ~2.5 to 4 μm for I^- diffusion at 120°C. Using the approximate diffusion length equation $x = (D_V t)^{1/2}$ we extract a volume diffusion coefficient of $D_V = 1.5\times10^{-11}\pm6\times10^{-12}$ cm^2/s. This diffusion coefficient is comparable to the diffusion coefficient extracted from the lateral diffusion study of $MAPbBr_3$ single crystals at 120°C ($D_V = 4.5\times10^{-11}$ cm^2/s). Given the charging of the single crystal samples and the lower sensitivity of 1D depth profiles, mainly due to a smaller number of analyzing frames during the data collection, compared to the lateral SIMS profiles we expect an underestimation of diffusion length in depth profile-based measurements. We believe this further shows the importance of the lateral diffusion geometry methodology developed in this work

because it reduces the occurrence of these artifacts, shortens the data acquisition time, and allows us to capture both volume and GB diffusions with higher precision and accuracy than depth profiles through bulk samples. In addition, with the ability to increase the number of analyzing frames in lateral geometry study, while keeping the measurement within a reasonable time frame to avoid beam instability, we can also achieve a higher signal/noise ratio which is particularly needed for GB diffusion regions.

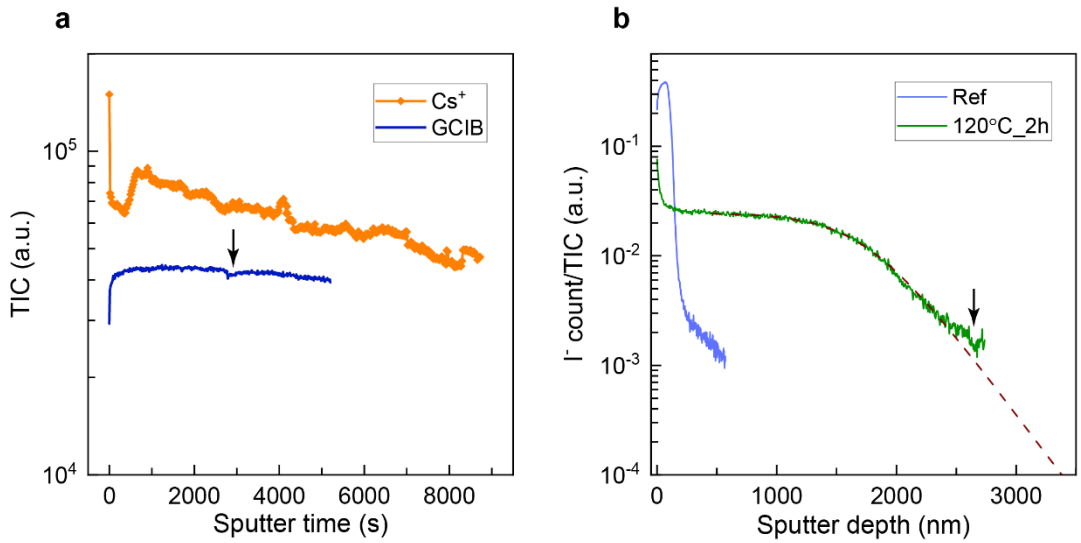

Fig. S6. a, 1D depth profiles of TICs of $MAPbBr_3$ single crystal samples with a 150 nm evaporated PbI_2 layer collected with Cs^+ and GCIB sputtering sources. Cs^+ (3keV-12nA) and GCIP (20 keV-10 nA) profiles were collected on ION TOF-SIMS V and PHI nanoTOF II systems, respectively. In both Cs^+ and GCIB cases, a 50×50 μm^2 and 500×500 μm^2 were selected as the analysis and sputtering areas, respectively. The back arrow on GCIB profiles points to the LMIG beam instability which causes a spike in profiles. **b**, depth profiles of reference (Ref) $PbI_2/MAPbBr_3$ and 120°C annealed samples. The Ref and 120°C annealed profiles were collected using Cs^+ and GCIB sputtering sources, respectively. The sputtering time to depth conversion was done by employing a stylus-based profilometer to measure the crater depth after sputtering. The dashed line shows a Boltzmann function fit used for extrapolation of the depth diffusion profile to the background level.

3. RSF calculation

To account for the matrix effect in SIMS profiles we prepared and measured a set of samples consisting of different amounts of iodine and bromine to investigate the matrix effect in these systems. Due to the similarity of the chemical structure of FA and MA-based perovskite we chose a FA-based mixed halide system for the matrix effect study. The selection of a FA-based mixed halide perovskite is based on the similarity between total ion count (TIC) normalized Br^- count in $MAPbBr_3$ and $FAPbBr_3$ (**Fig. S7**). To investigate the matrix effect and extract composition relative

sensitivity factor (RSF) we performed SIMS measurements on $FA_{0.85}Cs_{0.15}(I_yB_x)_3$ thin films (y = 1-x) with x values of 0, 0.001, 0.002, 0.004, 0.006, 0.008, 0.01, 0.02,0.04, 0.06, 0.08, 0.1, 0.2, 0.3, 0.4, and 0.5. Stock solutions of 1.0 M $FA_{0.85}Cs_{0.15}PbI_3$ and $FA_{0.85}Cs_{0.15}PbBr_3$ are made and mixed prior to thin film preparation in different rations to achieve desired compositions. To reduce the effect of experimental error during precursor mixing, in particular for the precursors with a small amount of x such as x = 0.001 we increase the total volume of the solution. For instance, for x = 0.001 precursor we mixed 2997 µl of $FA_{0.85}Cs_{0.15}PbI_3$ with 3 µl of $FA_{0.85}Cs_{0.15}PbBr_3$. We should note that all SIMS measurements in this work including the measurements in which we monitored the diffusion of foreign halides into host perovskite included a set of reference samples, e.g. a set of FACsRbI and $FAPbBr_3$ samples were loaded into ION TOF instrument in every measurement which we monitored I^- diffusion in $FAPbBr_3$ and vice versa. This allows us to account for LMIG current fluctuation at different measurement cycles and adjust the primary ion current which gives us a consistent total ion count across the reference.

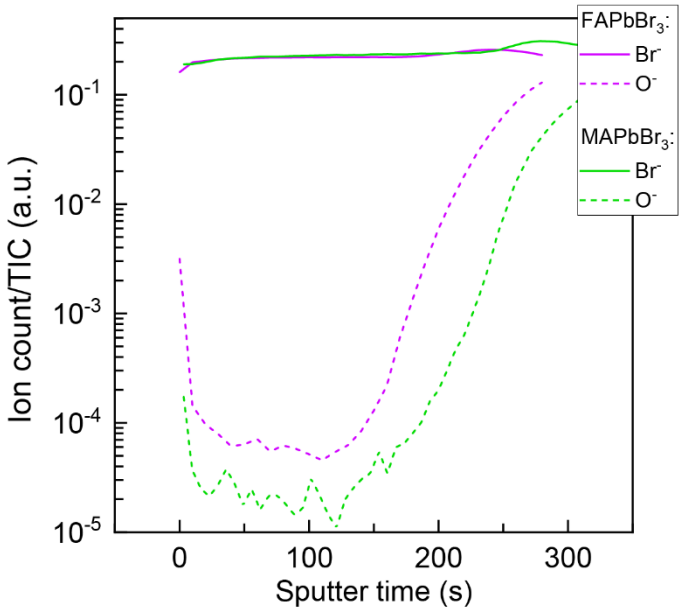

Fig. S7. TIC normalized Br^- counts in $MAPbBr_3$ and $FAPbBr_3$ 0.23±0.02 and 0.24±0.03, respectively. The increase in Br^- signal around 200 seconds of sputtering is due to a change in ion yield in presence of oxygen in SiO_2.

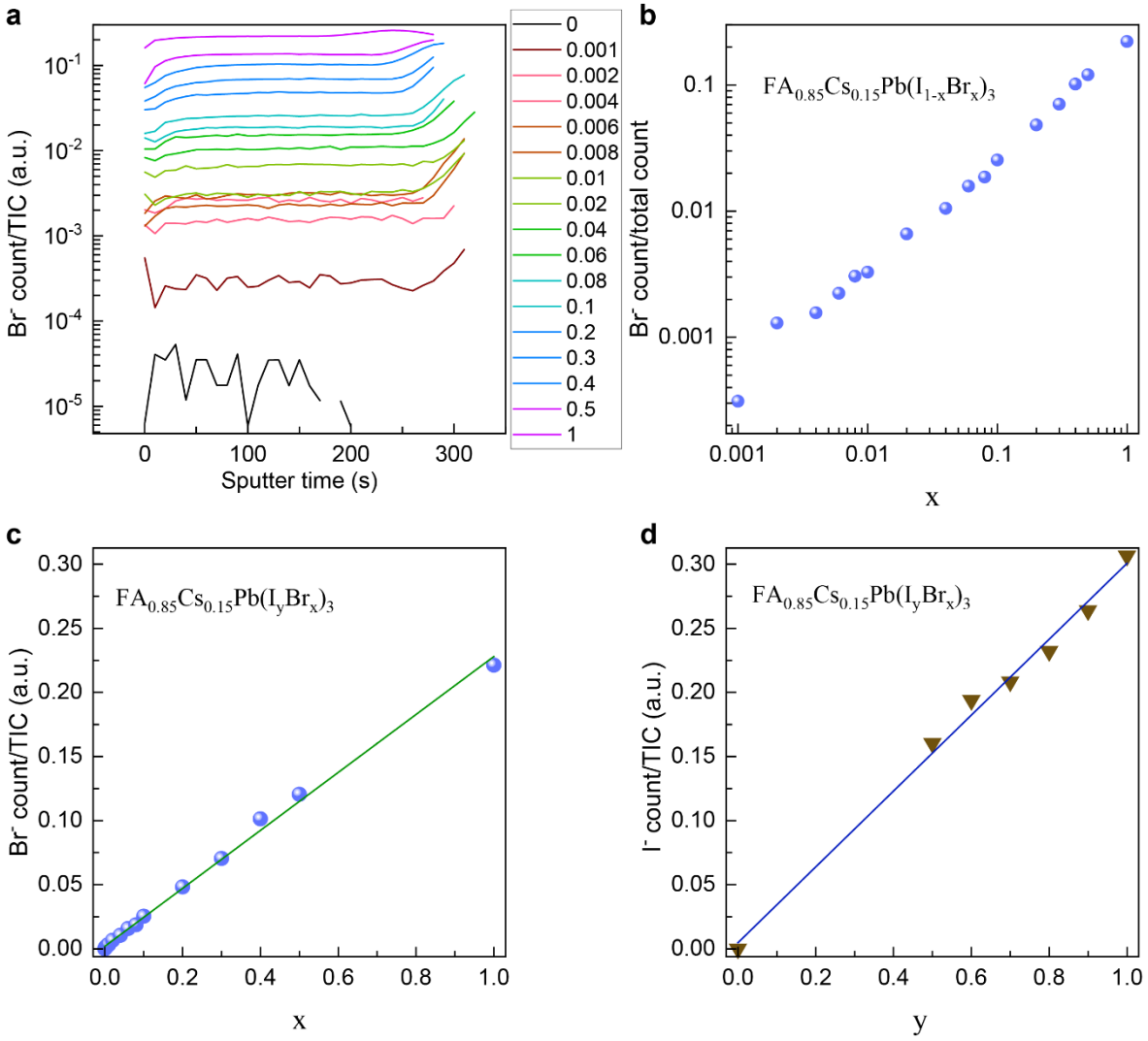

Fig. S8. **a**, 1D SIMS profiles of TIC normalized $^{79}Br^-$ (referred to as Br^-) count in FA-based mixed halide system $FA_{0.85}Cs_{0.15}Pb(I_yBr_x)_3$ with different amounts of Br^-. **b-c**, TIC normalized Br^- count in log-log and linear-linear scale, the green lines show the linear fit. **d**. TIC normalized I^- count in as a function $FA_{0.85}Cs_{0.15}Pb(I_yBr_x)_3$ of y, the line shows the linear fit to the data. The composition RSF factor for Br- and I^- in a MHP system can be calculated from the slop of the linear fit (RSF = 1/slope).

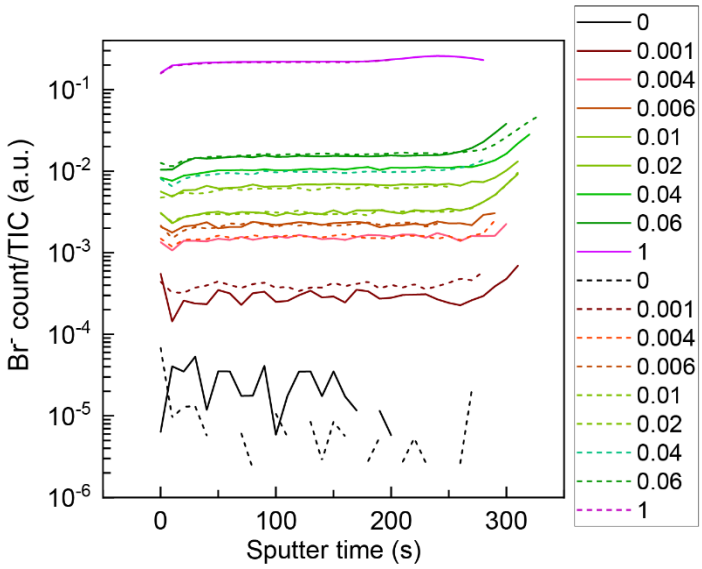

Fig. S9. 1D SIMS profiles of TIC normalized Br^- count in FA-based mixed halide system $FA_{0.85}Cs_{0.15}Pb(I_yBr_x)_3$ with different amounts of Br^- collected during two different sets of measurements on two different days. The reproducibility of TIC normalized Br^- signal shows that RSF factor calculated from 1D SIMS profile of the mixed halide system can be used for the count to composition conversion of the diffusion profiles collected during this study.

As can be seen from **Fig. S8**, the $^{79}Br^-$ signal shows a linear increase by increasing bromine composition in $FA_{0.85}Cs_{0.15}(I_yB_x)_3$. The RSF for the composition of $^{79}Br^-$ in $FA_{0.85}Cs_{0.15}(I_yB_x)_3$ using a 3 keV Cs^+ sputtering gun can be extracted from the slope of the linear fit (RSF = 1/slope). Due to similarity in mass abundances of stable Br^- isotopes ($^{79}Br^-$ and $^{81}Br^-$ with abundances of 50.68% and 49.31%, respectively) we use $^{79}Br^-$, referred to as Br^- hereafter unless otherwise mentioned, for RSF calculation and diffusion profiles. We extracted the composition RSF_{Br} for $^{79}Br^-$ to be 4.40, when corrected for the abundance of ^{79}Br (50.68%) we extract the total RSF of Br^- to be 2.23. Similar to bromine, the iodine signal also shows a linear increase when plotted against 1-x or y with a composition RSF_I of 2.94. The smaller RSF extracted for Br^- compared to I^- is consistent with a larger electron affinity of Br[3]. These RSFs are being used to convert the semi-quantitative SIMS results to quantitative composition profiles. To ascertain the reproducibility of the results a sub-section of the samples was measured on two different days (**Fig. S9**). As can be seen, the TIC normalized Br^- signal in reference and mixed halide samples show good reproducibility. Due to the similarity of the matrix between MA- and FA-based systems (organic cation, lead, and halide), RSFs extracted from FA and mixed cation systems are also used for iodine and bromine count to composition conversion in MA-based systems.

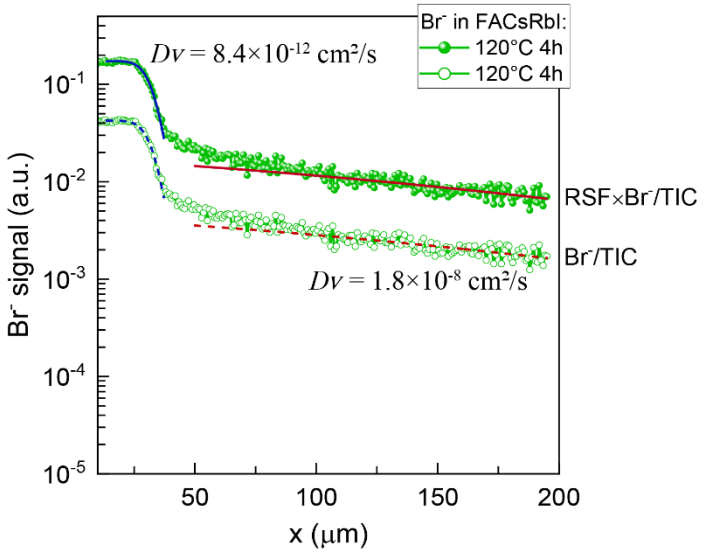

Fig. S10. D_V and D_{GB} fit to Br^-/TIC and RSF corrected diffusion profiles. The blue and red lines show the D_V and D_{GB} *erfc* fits, respectively. For a concentration-independent diffusion, *erfc* fit is the solution to a second order linear differential equation. As a result normalization of diffusion profile (RSF correction) by a constant number does not alter D_V and D_{GB} extracted from the fits.

4. Notes on diffusion

It is widely accepted that self-diffusion and foreign ion diffusion in MHPs are vacancy and defect mediated[4, 5]. And it has been shown that the diffusion coefficient in polycrystalline systems, in general, can be written as a product of a geometrical term ga^2, a correlation factor f, and the atomic jump rate, v^0. The correlation factor, in this case, represents the motion of atoms in a solid which is not free of memory effect. For a case of direct interstitial diffusion in which no vacancy is involved $f = 1$ and for the case of vacancy mediated diffusion $f < 1$. As a result, the temperature-dependent diffusion coefficient can be written as:

$$D = fv^0 ga^2 g_D \exp\left(\frac{G_D - G_B + G_M}{k}\right)$$

$$fv^0 ga^2 g_D \exp\left(\frac{S_D - S_B + S_M}{k}\right) \exp\left(-\frac{H_D - H_B + H_M}{kT}\right) = D_0 \exp\left(-\frac{E}{kT}\right) \qquad (1)$$

where G_D, H_D, and S_D, denote the free energy, enthalpy and entropy of defect formation. G_B, H_B, and S_B denote the binding free energy, enthalpy and entropy between forging ion and defect. And, G_M, H_M, and S_M, denote the free energy, enthalpy and entropy of motion for an exchange/migration. Due to the similarity of the perovskite compositions used in this study, we attribute the observed differences in the diffusion pre-factor (D_0) and activation energy (E) to the collective activation entropy and enthalpy and, in particular, to the entropy and enthalpy of defect formation.

5. *Harrison Classification*

Based on Harrison classification typical concentration profiles observed in polycrystalline metals or ionic crystals can be classified into three main types (Type A, B, and C)[6]. Type A concentration profiles are observed in samples annealed at elevated temperatures and for extended durations. They exhibit the coexistence of volume and GB diffusion behaviors throughout the sample, resulting in a diffusion profile that obeys Fick's law and is quantified by an effective diffusion coefficient (D_{eff}) that does not allow the two diffusion modes to be decoupled. Type B concentration profiles emerge in samples annealed at intermediate temperatures/durations and are ideal because they consist of two distinct parts: (i) a Gaussian or complementary error function (*erfc*) profile (depending on whether the source is finite or constant, respectively) representing the volume diffusion located near the diffusing ion source, and (ii) an exponential tail (when plotted against $x^{6/5}$, where x is the distance from the source, representing faster GB diffusion extending further from the source and therefore requiring a very thick sample given large diffusivities of halides. Type C profiles are observed in samples annealed at low temperatures for short durations and exclude any volume diffusion and also require very thick samples. These profiles are observed in samples with a very short annealing time or at a distance far from the source of foreign ions as diffusion takes place solely through GBs with minimal segregation and negligible penetration of diffusing atoms into the grains[7, 8]. The Fisher model of diffusion along GBs adopted by LeClaire to polycrystalline systems is employed to quantify both volume and GB diffusions[9, 10]. Due to the continuous diffusion of ions from the top layer and the overlap region into the host layer the lateral diffusion geometry and annealing conditions resemble those used in the constant source geometry.

The equation used in this work to fit the segregation region of the 1D SIMS profile can be written as

$$\delta s D_{GB} = 0.654\left(-\frac{\partial lnc(x)}{\partial x^{\frac{6}{5}}}\right)^{-\frac{5}{3}}\left(\frac{4D_V}{t}\right)^{\frac{1}{2}} \quad (2)$$

$$\delta s = 0.654\left(-\frac{\partial lnc(x)}{\partial x^{\frac{6}{5}}}\right)^{-\frac{5}{3}}\left(\frac{4D_V}{t}\right)^{\frac{1}{2}} D_{GB}^{-1} \quad (3)$$

$$\alpha = \frac{s\delta}{2\sqrt{D_V t}} \quad (4)$$

where δ is the grain boundary width, s is the segregation factor of the solute diffuser, D_{GB} is the GB diffusion coefficient, c is solute concentration as a function of penetration depth, x is the

penetration depth, and t is the diffusion/annealing time. In cases with $\alpha < 0.1$ a Type B diffusion is present, and an $\alpha > 10$ is associated with Type C diffusion[8, 11]. An interval value of α represents an intermediate regime in which both Type B and C (Type B/C) diffusion take place[8]. In order to examine the diffusion regime in the lateral halide diffusion study, we first fit the segregation regime using equation 2 when the logarithm of concentration profile (Ln(c)) is plotted against $x^{6/5}$ (**Fig. S11** two examples of fits using equation 2), this fit provides the first term in equation 3 (slope). Although s and δ can't be extracted separately, equation 2 allows us to extract the product of s and δ which is subsequently used in equation 4. Knowledge of the temperature-dependent GB width is required to be able to extract segregation factors in MHPs which is beyond scope of the current study. By using D_V extracted from volume diffusion fit and a range of D_{GB} reported for $MAPbI_3$ and mixed cation systems at different temperatures (e.g., 10^{-10}-10^{-9} cm^2/s at 100°C)[12-15]. we found that for all cases presented in this study $\alpha > 0.1$ ranged from 0.3 to 22. Subsequently, we used the exponential tail of the concentration profile to directly extract D_{GB}. One possible explanation for the presence of Type B/C in such a long-range diffusion profile could be a large GB width observed in MHPs compared to classic oxide and ceramic systems[11, 16, 17]. A larger GB width increases the product of $s\delta$. This subsequently pushes α to be in an intermediate Type B/C regime.

When using Equation 1 from the Main text to fit the volume diffusion portion of Type B/C it is also important to account for the contribution of GB concentration. To account for GB concentration in volume region, we simply add a y_0 constant value to *erfc*. function as a background concentration value. Meaning for a volume diffusion fit c(x) can be written as $c(x) = c_{V0} erfc\left(x - x0/2\sqrt{D_V t}\right)$. Single source assumption for both volume and GB dictates that both volume and GB fits have similar x_0, source displacement value. As a result, the fitted x_0 value extracted from the volume diffusion fit is used an input constant value for the subsequent GB fit. For the volume diffusion fits, the upper limit of the fitting range is more critical while in GB region the lower limit of the fitting range is more critical. For instance, in **Fig. 2a-b** the range of volume diffusion fit is about 45 μm, from 21 to 66 μm. Changing the lower limit of the fitting range has no significant effect on volume diffusion fit while the upper limit of the fit should be chosen in a way that the volume diffusion fit does not extend into segregation or GB regions. Due to the same reason, the lower limit of the fitting range is more important in GB diffusion to avoid the fit being extended into segregation and volume regions. Since the boundary between segregation and GB regions is not as clear as the boundary between volume and segregation regions the GB fits have

been done on several different fitting ranges (3-4 different ranges by changing the lower limit value) and the D_{GB} values are averaged over these different ranges. This leads to a larger error bar on extracted D_{GB}s compared to D_Vs. Our results also show that the range of integration along the y-axis does not affect the diffusion profile and subsequent fit. It is worth noting that, the length scale of Type B profiles is orders of magnitude larger than the thickness of films, highlighting the near impossibility of creating meaningful halide diffusion profiles along the depth of application-relevant thin films.

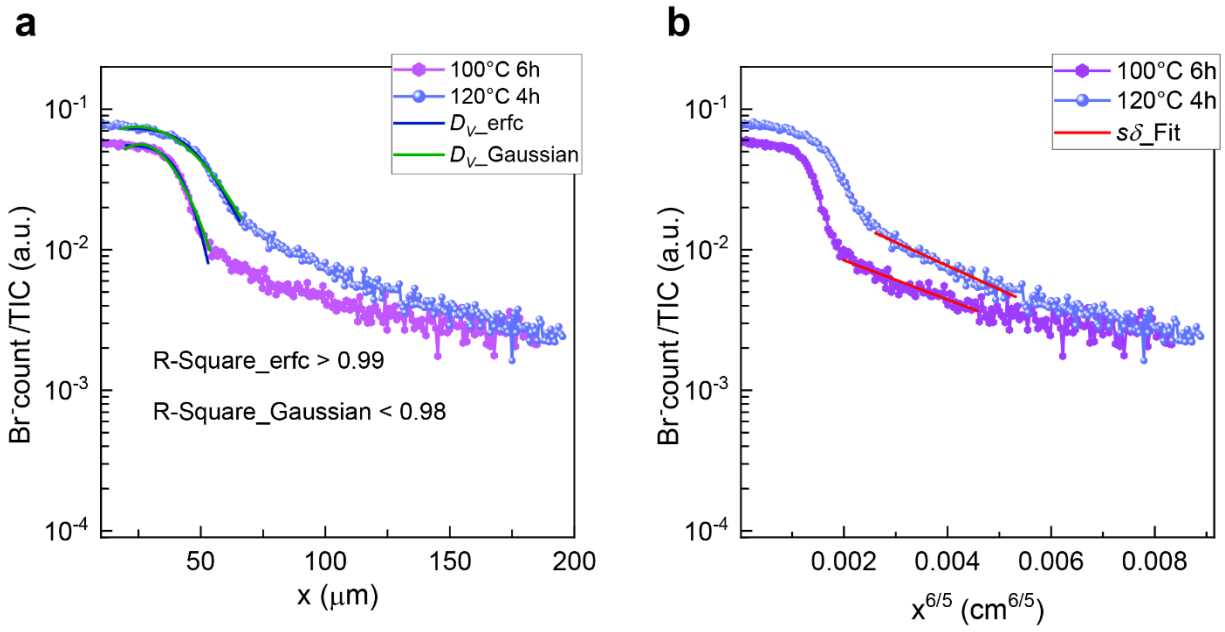

Fig. S11. **Finite versus constant source fit comparisons**. 1D SIMS profiles of Br^- diffusion into $MAPbI_3$ at two different temperatures 100 and 120 °C plotted against **a**, x and **b**, $x^{6/5}$.

Increasing the annealing duration at a certain temperature shows both volume and GB compositions of foreign ions increasing with respect to the host ions (see **Fig. S12**). Nevertheless, detailed analysis shows no significant changes in the volume and GB diffusion coefficients as a function of annealing time.

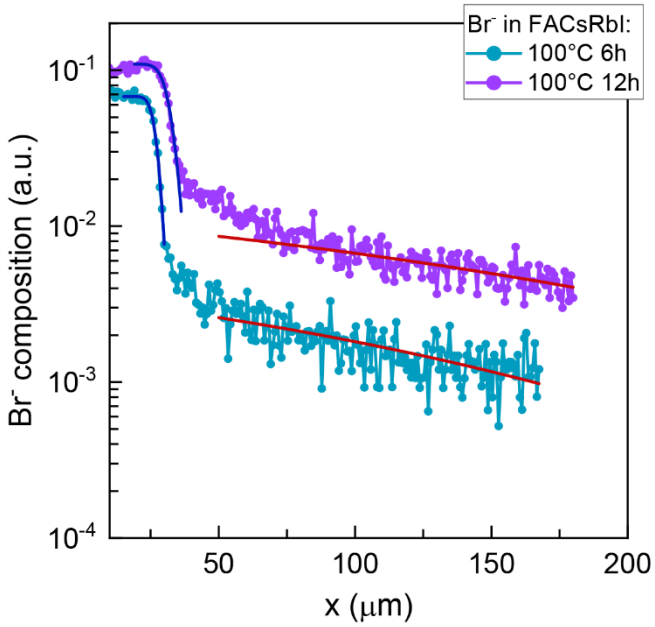

Fig. S12. 1D SIMS profiles of Br^- diffusion into FACsRbI MHP at 100°C for two different time duration. 1D SIMS profiles plotted against x and. The D_V and D_{GB} extracted from each profile are reported in **Table S1**.

Table S1. D_{GB} and D_V were extracted from *erfc* fit for the diffusion of Br- into FACsRbI.

	D_{GB} (cm^2/s) $\times 10^{-9}$	D_V (cm^2/s) $\times 10^{-12}$
100°C_6h	4.8 ± 0.8	1.3 ± 0.2
100°C_12h	4.2 ± 0.6	1.6 ± 0.3

6. PL microscopy

PL microscopy is a powerful technique for the investigation of ion migration within the perovskite lattice, while extra care needs to be taken when this method is being used for ion migration studies along the GBs. As such, a long range GB diffusion can remain invisible to PL due to a lack of radiative recombination and/or extremely low composition of ions/defects migrating along the GBs[18]. Subsequently, our results also point to the limitation of PL microscopy in the investigation of ion migration along the GBs of polycrystalline MHPs.

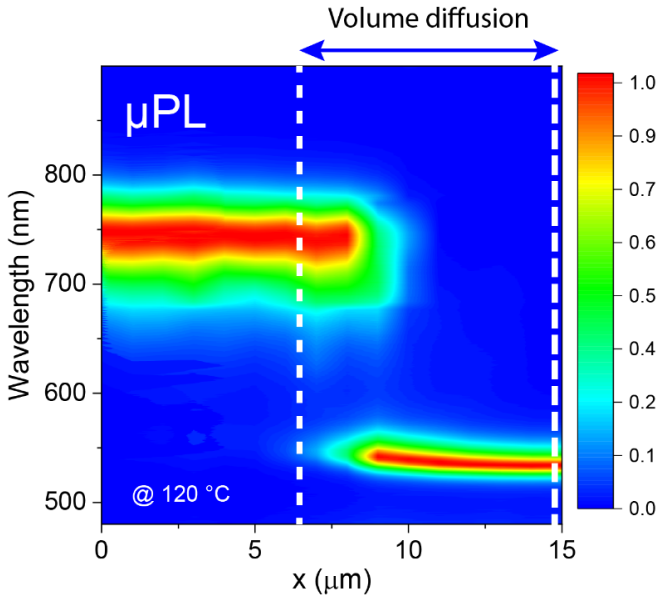

Fig. S13. μPL map of I^- diffusion in the host $MAPbBr_3$ film. The laminated samples were annealed for 2 hours at 120°C prior to the measurement.

7. X-ray photoemission spectroscopy

X-ray photoemission spectroscopy (XPS) was also used to monitor the lateral distribution of iodine in FAPbBr3 after being in contact with FACsRbI at 120°C for 2 hours (see **Fig. S14-16**). XPS results show a gradient in iodine count from the overlap region into the diffusion region. Interestingly, the gradient in iodine count also coincides with a gradient in metallic lead Pb^0 signal that was initially absent in the control $FAPbBr_3$ sample. As a result, we associate the Pb^0 and its correlation with the iodine concentration gradient to the formation of PbX_2, and in particular PbI_2, in the overlap region and the area of the diffusion profile with a high content of iodine[19]. PbI_2 formation in the overlap region of FAPbBr3/FACsRbI is also confirmed using X-ray diffraction (XRD) and SEM as can be seen in **Fig. S17.**

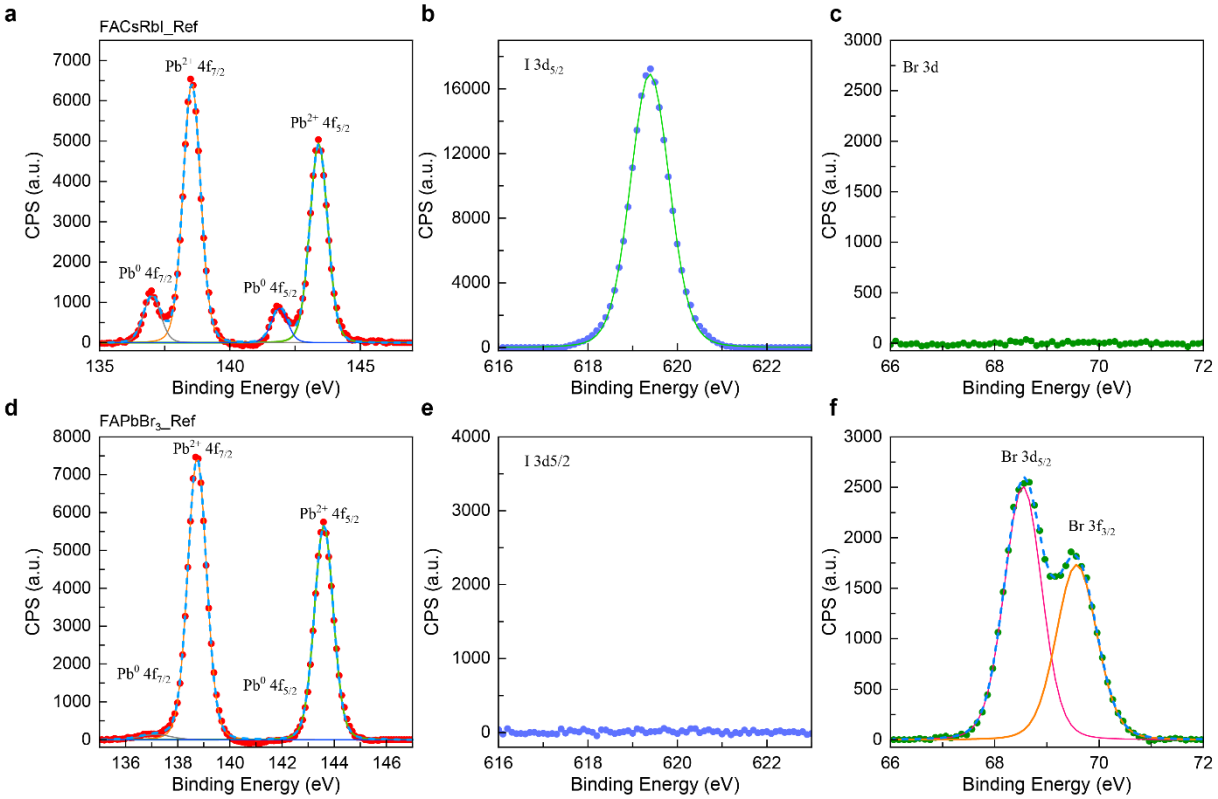

Fig. S14. a, Pb 4f **b**, I 3d, and **c**, Br 3d XPS spectra of control FACsRbI sample. **d**, Pb 4f **e**, I 3d, and **f**, Br 3d XPS spectra of control $FAPbBr_3$ sample.

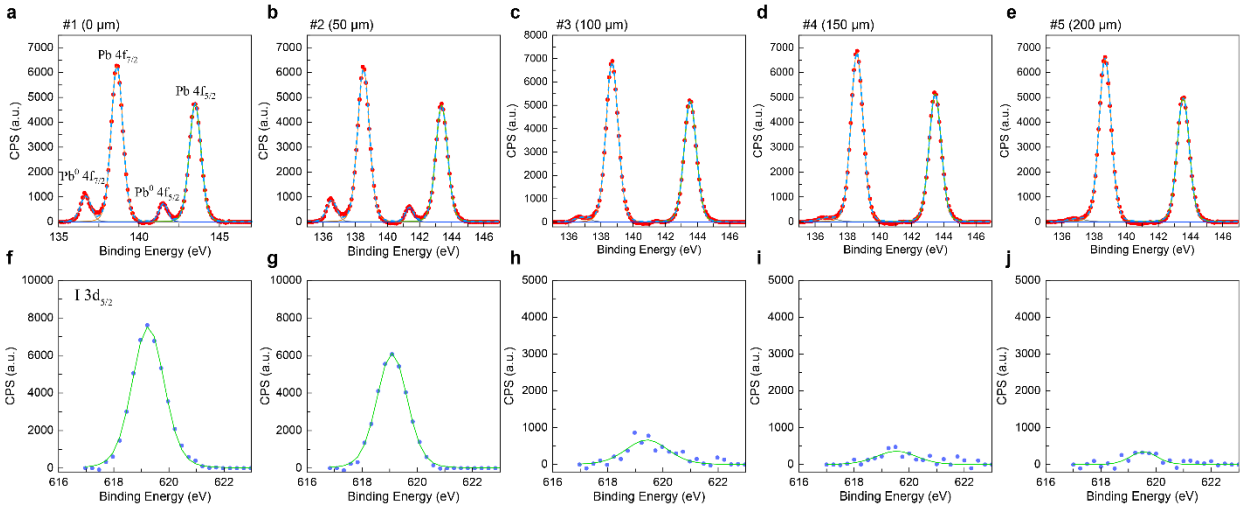

Fig. S15. a-e, Pb 4f and **f-j**, I 3d spectra of $FAPbBr_3$/FACsRbI sample after annealing at 120°C for 2 hours as a function of position. $FAPbBr_3$ is the host system. x = 0 μm represents a point in overlap reigon of diffusion while x = 200 μm represents a point at GB diffusion region. A relatively large spot size (20 μm) is used to collect this set of measurements to increase the signal/noise.

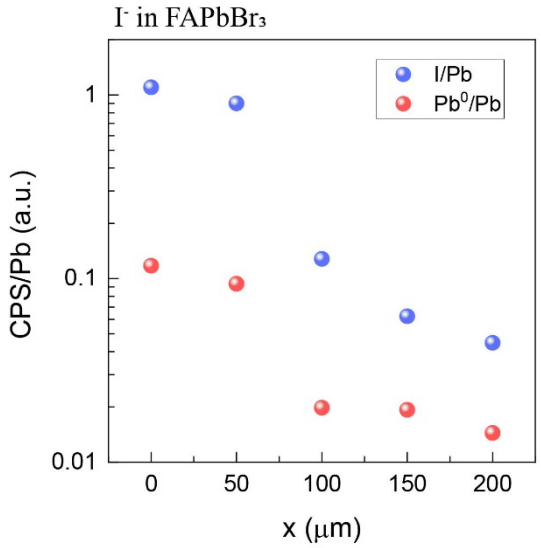

Fig. S16. Pb 4f normalized I 3d and Pb^0 count per second (CPS) as a function of position in $FAPbBr_3$/FACsRbI sample after annealing at 120°C for 2 hours as function of position. $FAPbBr_3$ is the host system. x = 0 μm represents a point in overlap region of diffusion while x = 200 μm represents a point at GB diffusion region.

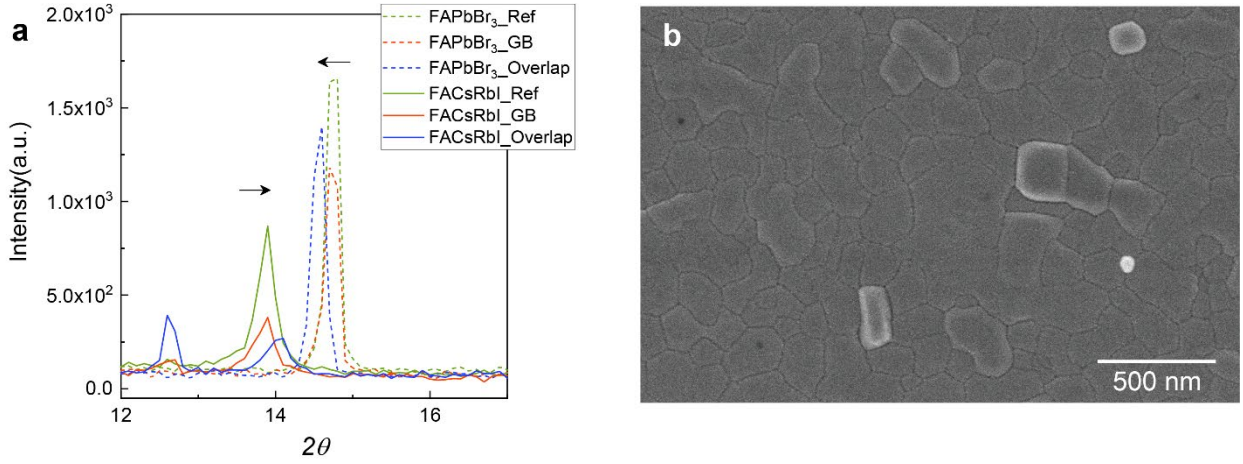

Fig. S17. a, XRD results of overlap and GB regions in FAPbBr3 and FACsRbI samples after diffusion of I^- and Br^-, respectively. The foreign halide diffusion experiment was carried out at 120°C for 4 hours. **b**, SEM image of overlap region in $FAPbBr_3$ samples after being in contact with FACsRbI at 120C for 4 hours. The grains with white color are associated with lead-halide PbI_2 phases in MHP systems. The formation of the PbI_2 phase can also be observed in the XRD results (2θ ~ 12.6°) and Pb^0 signal in XPS.

8. I^- diffusion in $MAPbBr_3$ single crystal

To validate the proposed volume diffusion framework, we investigate the diffusion of I^- into MAPbBr3 single crystals (SCs) (see **Fig. S18**). We formed a lateral diffusion geometry by vacuum

evaporating a 150 nm film of PbI_2 through a shadow mask on the surface of mechanically polished MAPbBr3 SCs (see Methods section for more details). The I^- diffusion into $MAPbBr_3$ SC follows an identical volume diffusion mechanism as in thin films and forms a pure volume diffusion concentration profile that is modeled similarly to the profile in the polycrystalline films. The SIMS analysis of I^- diffusion in SC shows that the foreign halide signal quickly drops to the background level beyond the volume diffusion region (**Fig. S19**). This is consistent with the classification of ion diffusion in polycrystalline versus SC samples. As a result, it can be concluded that the lack of a long-range exponential tail in I^- ions diffusion into the SC is due to the lack of grains and GBs in SCs. Interestingly, the SC diffusion results reveal that I^- ions diffuse in the SC with a volume diffusion coefficient 3-4 times larger than in thin films. This points to the important role played by the microstructure and, in particular, by the presence of GBs, which can act as point defect sinks[18, 20] and which we will show also appear to influence the volume diffusivity. Given the low activation energy/fast diffusion of ions on GBs, we infer that the transfer of ions from one grain to the neighboring grains (volume diffusion) can be hindered due to the preference of ions to diffuse on high energy GBs. A faster ion/defect migration in a SC compared to thin films during a defect healing process was also observed by Abate and co-workers[18]. In light of the differences observed in the volume diffusion of iodine $D_V(I^-)$ in thin film and SC MHPs, one can expect that grain heterogeneity also affects the volume and GB diffusion properties in MHPs. This can happen, for instance, when intragrain defects act as pathways with different morphological and energetic properties for ion diffusion. Identifying the correlation between intragrain structures with volume and GB diffusions begs for nanoscale studies in the future with tools that can resolve and quantify intergrain as well as intragrain diffusion behaviors.

Our results confirm that the fast moving ions signature observed in SIMS profiles and transient based measurements of polycrystalline MHP devices belongs to halide ions moving along GBs with two to five orders of magnitude diffusivity compared to volume. Moreover, we show that the presence of GBs in MHPs slows down volume diffusion (smaller D_V in thin films compared to SC) through mechanisms that need further elucidation. This slowdown is not at all equivalent to a total suppression of ionic movement along GBs. Instead, the presence of GBs in polycrystalline thin films reduces D_V while GBs simultaneously act as the faster ionic diffusion channel in these systems ($D_{GB} >> D_V$).

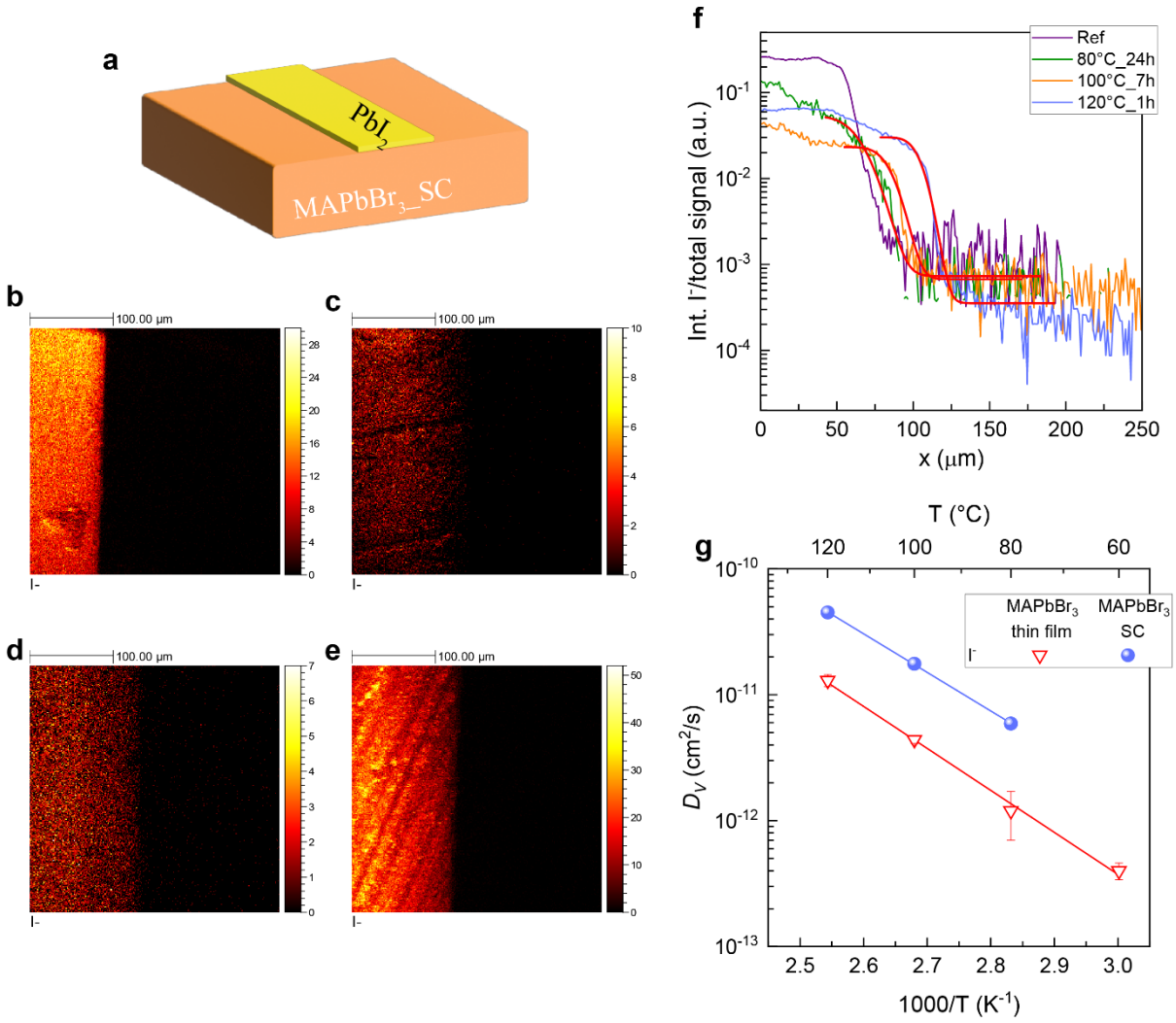

Fig. S18. a, Schematics of evaporated PbI_2 on $MAPbBr_3$ SC as a source for the diffusion of I^- into $MAPbBr_3$. **b-e**, I^- 2D SIMS images of the reference and annealed samples at three different temperatures. **f**, semi-quantitative integrated 1D SIMS profile of I^- diffusion in $MAPbBr_3$ SCs. The red lines show the *erfc* fit to the diffusion profiles. I^- diffusion coefficients as a function of 1000/T in thin film vs SCs. 500×500 μm^2 and 300×300 μm^2 raster sizes were used as sputtering and analyzing areas, respectively. Each sample was sputtered for 100 seconds, similar to the thin film analysis the data points covering the first 10-15 s were excluded to avoid surface effects and beam instability region. **g**, volume diffusion as a function of inverse temperature. The solid lines show the Arrhenius fit to the data. Data are presented as the fitted values for D_V extracted from Equation 1 ± standard error of the fit. The larger D_V in SC compared to polycrystalline thin film is mainly due to the smaller volume activation energy E_V in SC *versus* thin films (0.59 eV *versus* 0.66 eV).

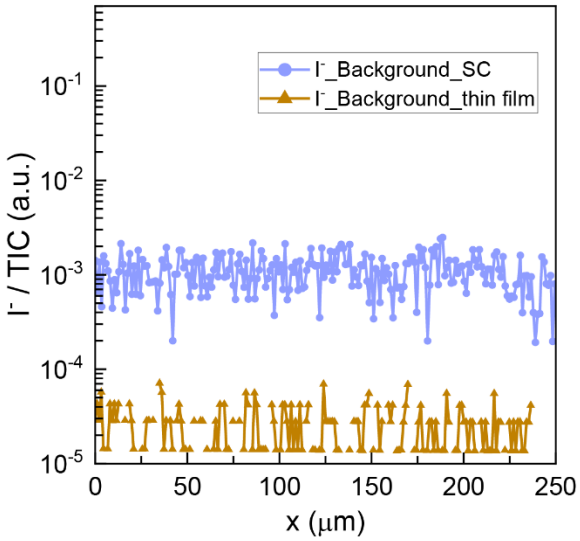

Fig. S19. I^- background signal in SC and thin film of $MAPbBr_3$. The background signals are not RSF corrected.

9. Note on PL and Superoxide

We monitored the superoxide generation yield in the overlap region of two different host FACsRbI samples after being in contact with $FAPbBr_3$ at 120°C for 10 seconds and 2 hours. The former is representing GB region in the lateral diffusion profile and the latter represents a volume/exchange diffusion region (see **Fig. S18**). While 10 seconds annealed samples show no changes in superoxide generation yield compared to control FACsRbI samples, the superoxide generation yield is increased 2 hours annealed sample (mixed halide). On the other hand, steady state and time resolved PL (TRPL) show an increase in PL intensity and carrier lifetime, respectively, for 2 hours annealed samples. This points to a smaller defect density in 2 hours annealed samples. Due to the observed increase in carrier lifetime and PL intensity in 2 hours annealed samples, we associate the increase in superoxide generation yield in this sample to the formation of PbI_2 due to prolong annealing[21, 22].

In order to compare the effect of volume and GB diffusion on carrier lifetime and defect density, we prepared two sets of FACsRbI samples in contact with $FAPbBr_3$ for two different time scales, 10 seconds vs 2 hours annealed at 120°C. In this experiment, we prepared the samples such that $FAPbBr_3$ is fully in contact with FACsRbI (overlap region). This allows us to perform time-resolved PL (TRPL) and superoxide measurements on the same set of samples to monitor the possible correlation between carrier lifetime and vacancy in samples with a foreign halide. Due to

the orders of magnitude larger D_{GB} compared to D_V it can be assumed with high confidence that at a very short annealing time, namely 10s, Br^- ions diffuse along the GB while diffusion into the bulk requires a longer annealing time. On the other hand, at a longer annealing time density of Br^- ions in the host FACsRbI films is mainly dominated by diffusing in the bulk of FACsRbI. As a result, these samples can be regarded as the diffusion architectures that represent GB and volume diffusion regions in a lateral diffusion study. To confirm this, we performed SIMS measurements on the 10 seconds and 2 hours ion exchanged samples. The Br^- counts in 10 seconds and 2 hours annealed samples are comparable to the Br^- counts in the GB, and the volume regions of the lateral diffusion.

First, we monitored the superoxide generation yield in the overlap region of these two different host FACsRbI samples after being in contact with $FAPbBr_3$ at 120°C for 10 seconds and 2 hours (see **Fig. S20**). While 10 seconds annealed sample shows no changes in superoxide generation yield compared to control FACsRbI samples, the superoxide generation yield is increased in 2 hours annealed sample. On the other hand, steady state and time-resolved PL (TRPL) show an increase in PL intensity and carrier lifetime, respectively, for 2 hours annealed samples (see **Fig. S21**). This points to a smaller defect density in 2 hours annealed sample. Such an increase in radiative recombination in mixed halide (overlap region in this case) systems compared to single halide MHP has been observed in mixed halide FACsMA[23]. We should note that while steady PL and TRPL results show an increase in PL intensity and carrier lifetime (smaller defect density), respectively, as mentioned before the superoxide measurement of 2 hours annealed sample shows an increase in superoxide generation yield which points to higher defect densities. We attribute this apparent disagreement to the formation of PbI_2 phases in 2 hours annealed samples that was shown to be correlated with an increase in superoxide generation yield[21, 22]. As a result, we can conclude that, while volume diffusion of foreign halides in the host perovskite leads to a decrease in defect density, GB diffusion of such ions does not alter the defect landscape of the host perovskite system.

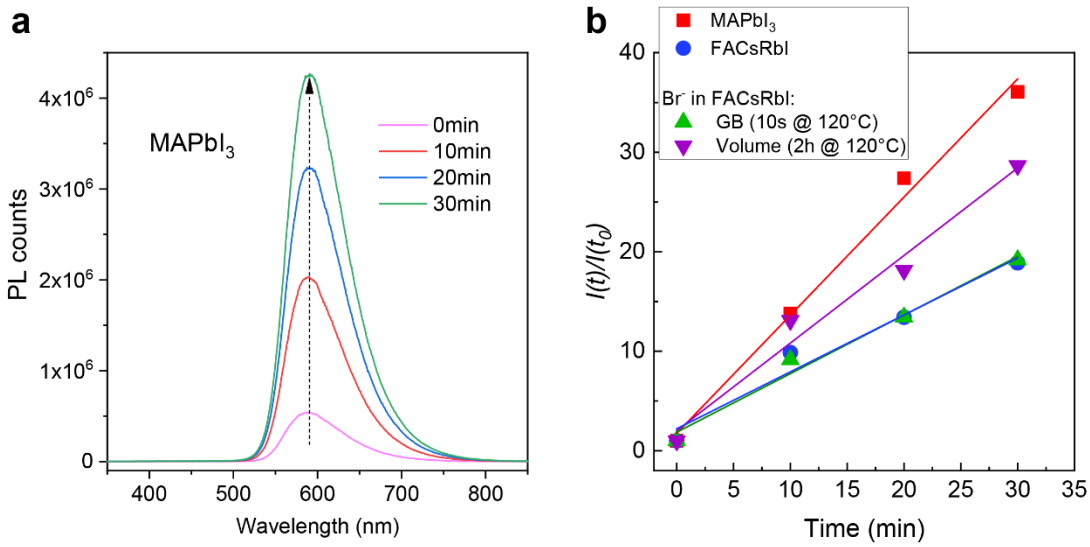

Fig. S20. PL of probe solution (0.01 mg/ml solution of dihydroethidium in chlorobenzene) as a function of aging time of perovskite under continuous white light illumination (0.015 sun) and constant oxygen flow. The PL spectra were collected using an excitation wavelength of 520 nm with 2.4 $mJcm^{-2}$ power. **b**, yield of superoxide generation for $MAPbI_3$, and FACsRbI control samples, and Br^- diffused FACsRbI thin films after being in contact with $FAPbBr_3$ for 10 seconds and 2 hours. $FAPbBr_3$ films were coated on SEBS to achieve good contact with FACsRbI and $FAPbBr_3$ thin films and uniform lateral distribution of Br^- in FACsRbI samples.

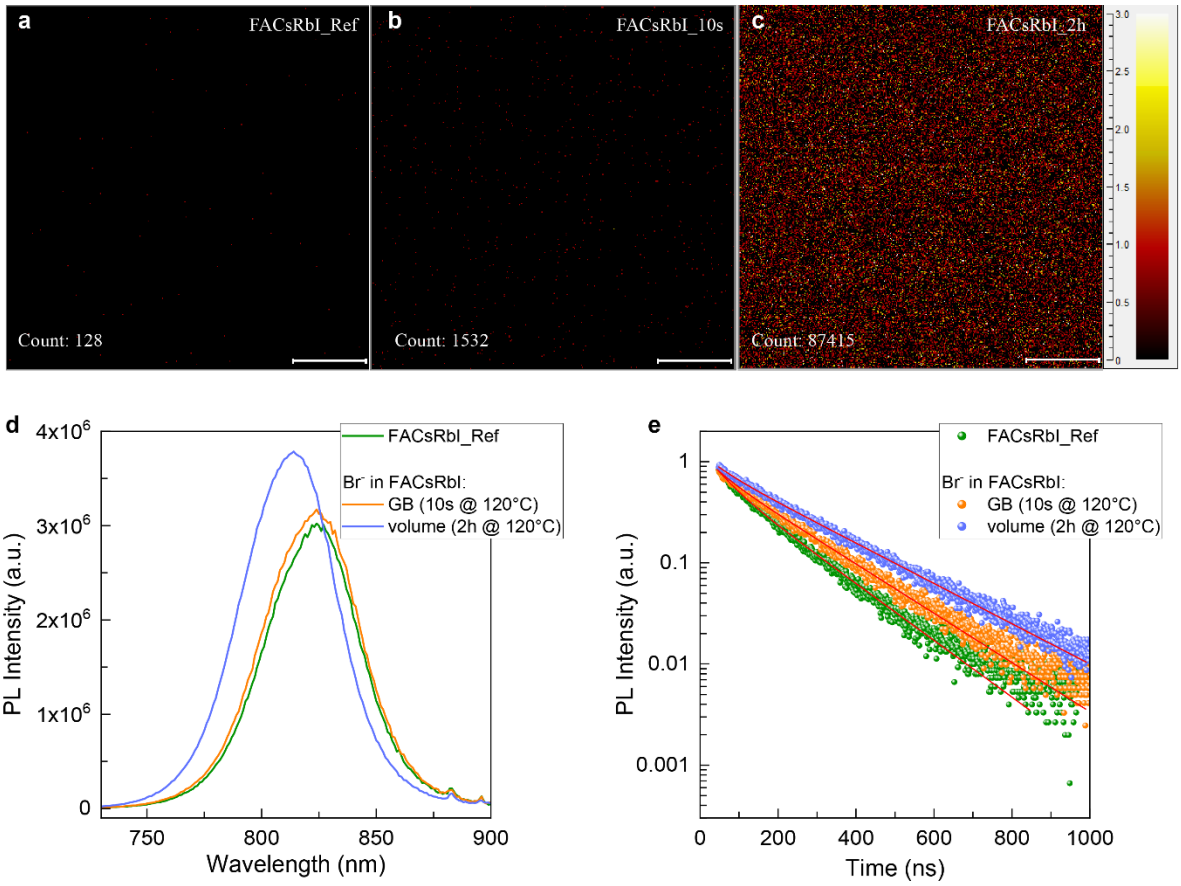

Fig. S21. **a-c**, 2D SIMS images of Br^- in FACsRbI control, and Br^- diffused FACsRbI thin films. The Br^- count in both 10 seconds and 2 hours annealed samples are more than the control samples. Scale bars are 10 µm. 2D SIMS images are collected using PHI nanoTOF at PSU. Steady-state PL **d**, and time-resolved PL (TRPL) **e**, of control and diffusion samples. TRPL spectra were collected at peak wavelengths. The PL intensity of Br^- diffused samples after 2 hours increases with respect to the control and 10 seconds annealed samples that point to lower defect densities in 2 hours samples. The blue shift in the PL peak of 2 hours samples also points to the diffusion of Br^- ions into FACsRbI lattice. While the lack of such a shift in 10 seconds annealed samples show that the majority of the Br^- ions in this film are located on GBs. FACsRbI shows a biexponential decay with fast (τ_1 = 48 ns) and slow (τ_2 = 134.7 ns) components. Whereas in 10 seconds and 2 hours samples we observe a slight increase in slow decay τ_2 = 179 and 209 ns, respectively, while the fast decay component does not show a significant change τ_1 = 46 and 50 ns, respectively.

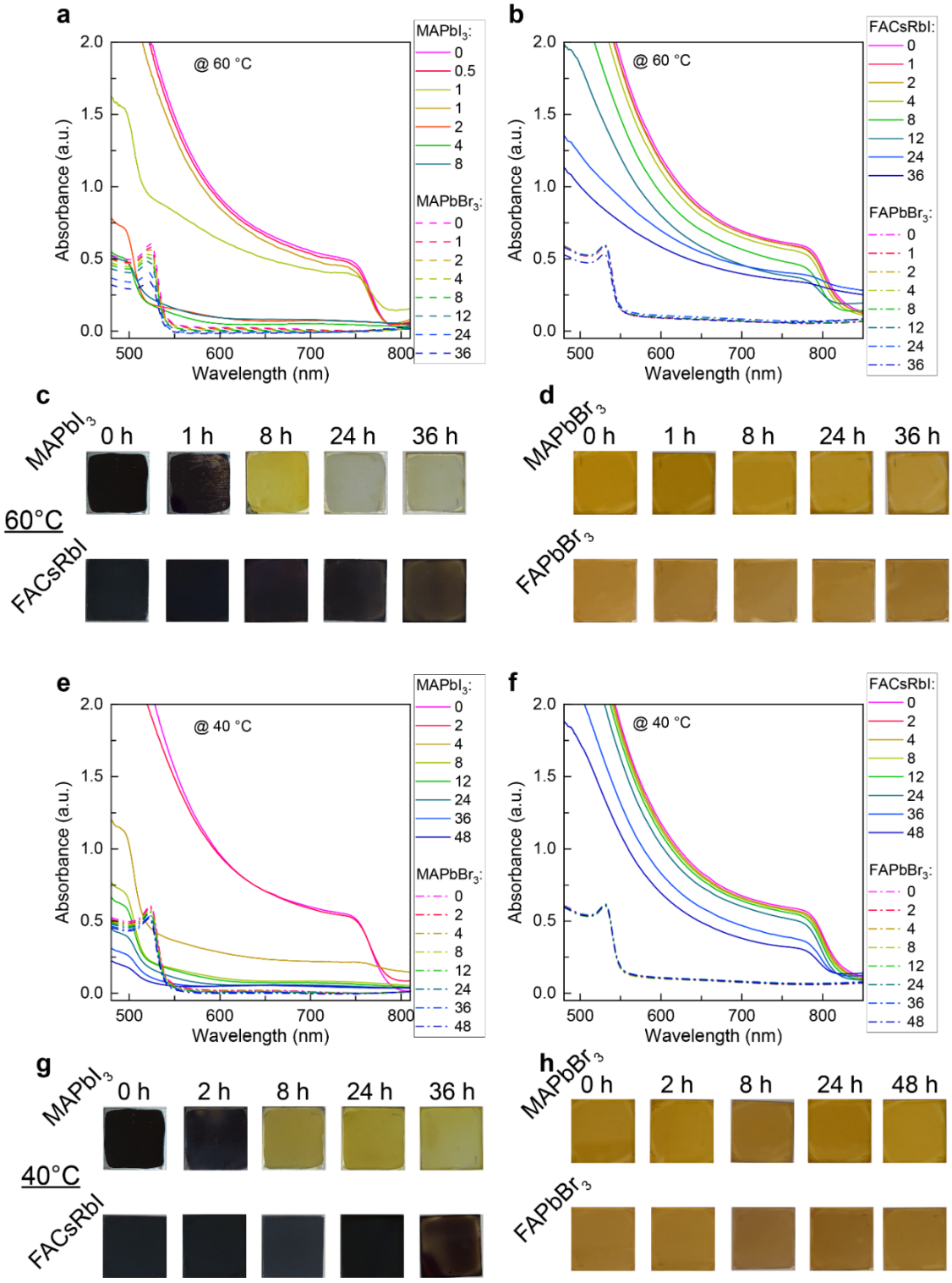

Fig. S22. **a-b,** and **e-f,** UV-Vis spectrum of $MAPbI_3$, $MAPbBr_3$, FACsRbI, and $FAPbBr_3$ exposed to white light with 25 mW/cm^2 power at two different temperatures 60 and 40 °C, respectively. The numbers on the legends represent the illumination time in hours. **c-d,** and **g-h,** $MAPbI_3$, $MAPbBr_3$, FACsRbI, and $FAPbBr_3$ after light degradation study as a function of time. Meanwhile, it can be seen that both of the bromide

systems have better stability compared to iodide systems. We associate the slower degradation in bromide systems to a combination of factors i) smaller D_V, ii) smaller size of bromide compared to iodine vacancies which lead to slower diffusion of oxygen through the grains, and iii) a lower density of electrons, needed for superoxide formation, in Br-based samples due to their larger bandgap.

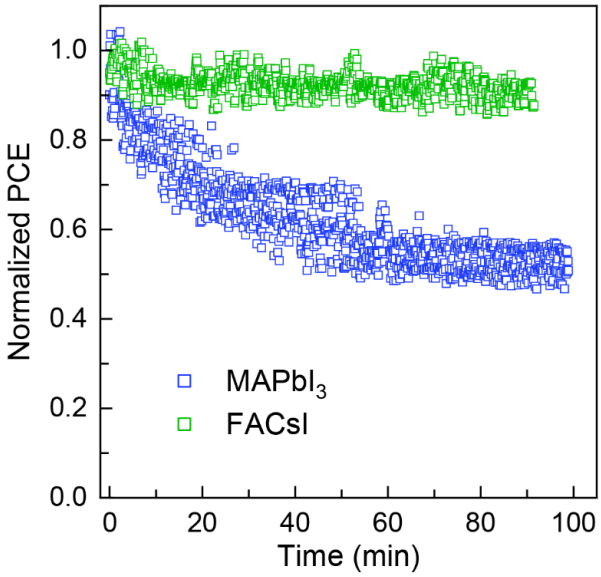

Fig. S23. Maximum power point tracking $MAPbI_3$ and FACsI unencapsulated devices collected at relative humidity < 30% at a temperature of 30-40°C.

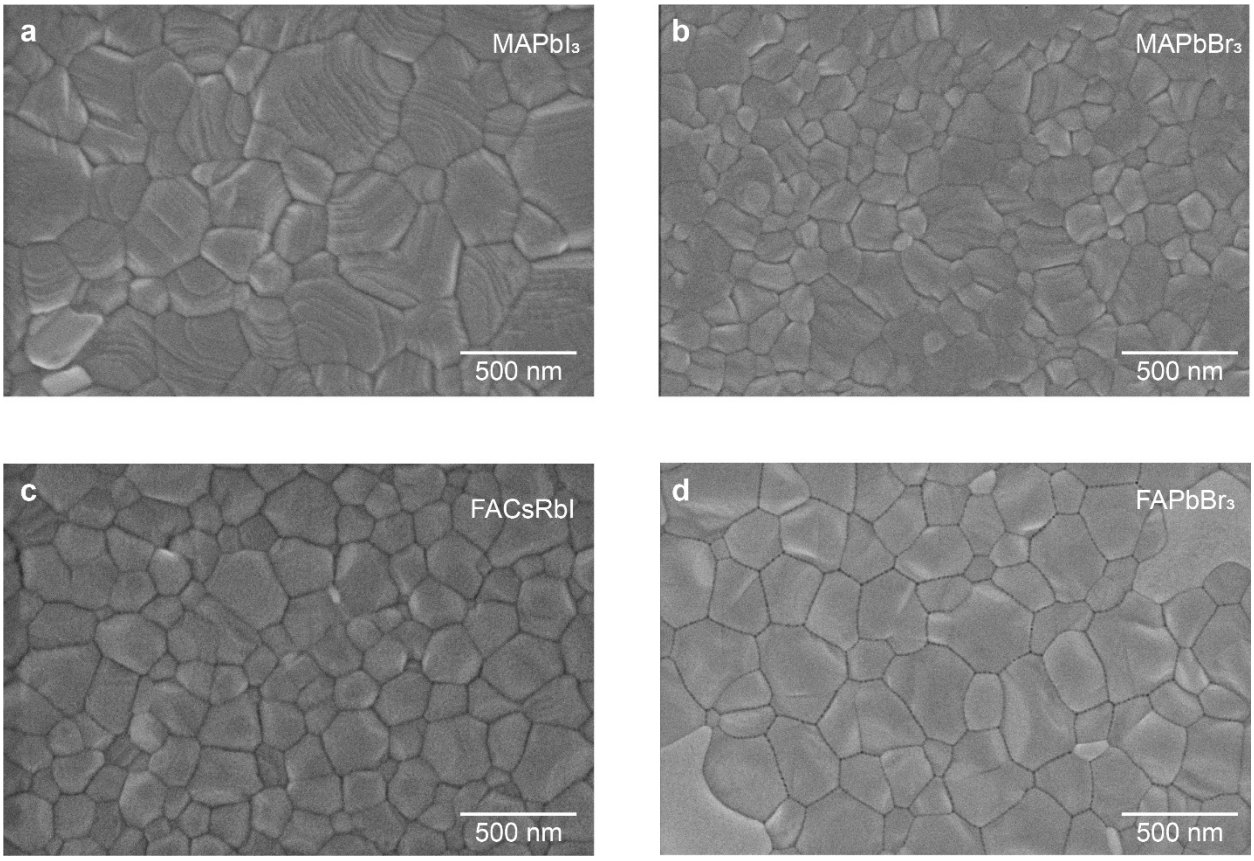

Fig. S24. Top-view SEM images of **a**, $MAPbI_3$ **b**, $MAPbBr_3$ **c**, FACsRbI, and **d**, $FAPbBr_3$. $MAPbI_3$ and $FAPbBr_3$ thin films have the largest grain size ranging from ~200 um to 500 um but given that these two systems show drastically different volume and GB diffusivities we can conclude that the observed differences in diffusivity of halides in MHPs compositions studied here are not due to the different grain sizes in these systems.

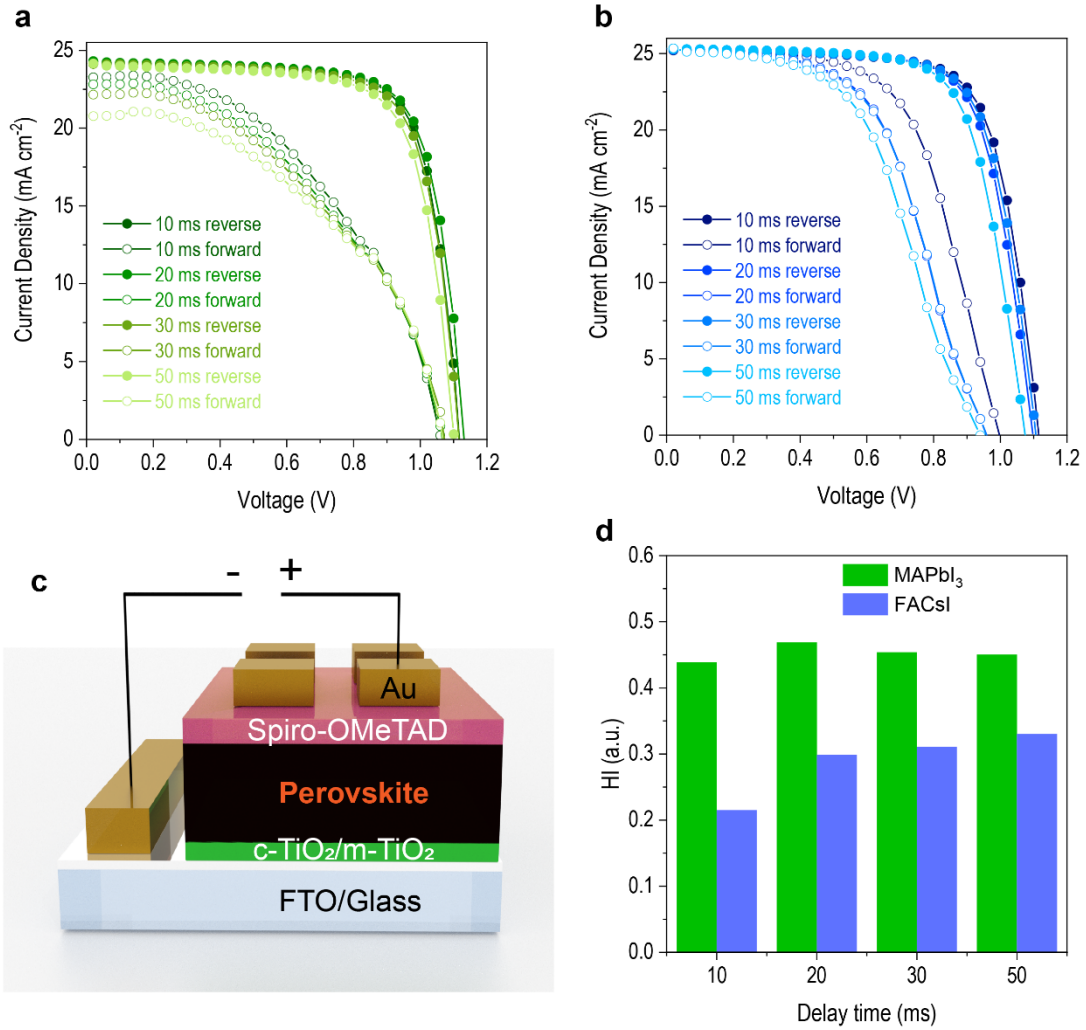

Fig. S25. **a-b,** *J-V* curves of $MAPbI_3$ and $FA_{0.85}Cs_{0.15}PbI_3$ (FACsI) PVs, respectively, at different scan rates (the delay time from 10 to 50 ms is defined by a pre-programmed voltage step of 0.5 V within the software, corresponding to 50 mV s^{-1} to 10 mV s^{-1}, respectively). **c,** schematic of completed n-i-p devices. **d**, Hysteresis index (HI) calculated for $MAPbI_3$ and FACsI devices[24].

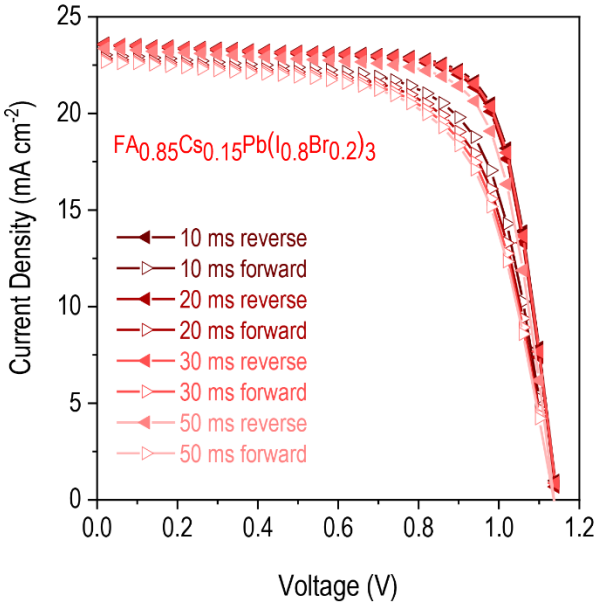

Fig. S26. *J-V* curves of mixed halide mixed cation devices in forward and reverse scans with different scan rates.

Table S2. Photovoltaic characteristics of fresh $MAPbI_3$ devices in reverse and forward scans (the delay time from 10 to 50 ms is defined by a pre-programmed voltage step of 0.5 V within the software, corresponding to 50 mV s^{-1} to 10 mV s^{-1}, respectively). The standard deviation of PCEs is based on at least ten different devices.

$MAPbI_3$	10 ms	20 ms		30 ms		50 ms		
	reverse	forward	reverse	forward	reverse	forward	reverse	forward
J_{SC} (mA cm^{-2})	24.18	23.21	24.25	22.82	24.12	22.17	24.02	20.96
V_{OC} (V)	1.12	1.07	1.13	1.07	1.11	1.07	1.10	1.07
FF (%)	74.4	45.8	74.1	44.4	73.4	45.3	72.5	47.1
PCE (%)	20.35 ± 0.98	11.46 ± 2.51	20.41 ± 0.88	10.75 ± 2.89	19.66 ± 0.96	10.61 ± 2.97	19.22 ± 1.05	10.41 ± 2.72
HI	0.44		0.47		0.45		0.45	

Table S3. Photovoltaic characteristics of fresh $FA_{0.85}Cs_{0.15}PbI_3$ devices in reverse and forward scans. The standard deviation of PCEs is based on at least ten different devices.

$FA_{0.85}Cs_{0.15}PbI_3$	10 ms	20 ms	30 ms	50 ms

	reverse	forward	reverse	forward	reverse	forward	reverse	forward
J_{SC} (mA cm^{-2})	25.2	25.24	25.26	25.31	25.25	25.28	25.31	25.32
V_{OC} (V)	1.11	1.04	1.1	1.00	1.11	1.0	1.07	0.98
FF (%)	72.3	60.7	71.2	54.8	71.7	54.7	70.2	51.6
PCE (%)	20.31 ± 0.72	15.87 ± 1.96	19.71 ± 0.82	13.75 ± 2.11	20.15 ± 0.93	13.56 ± 2.21	19.09 ± 0.88	12.58 ± 1.93
HI	0.22		0.30		0.31		0.33	

Table S4. Photovoltaic characteristics of fresh $FA_{0.85}Cs_{0.15}Pb(I_{0.8}Br_{0.2})_3$ devices in reverse and forward scans. The standard deviation of PCEs is based on at least ten different devices.

$FA_{0.85}Cs_{0.15}Pb(I_{0.8}Br_{0.2})_3$	10 ms	20 ms		30 ms		50 ms		
	reverse	forward	reverse	forward	reverse	forward	reverse	forward
J_{SC} (mA cm^{-2})	23.6	23.0	23.5	22.9	23.4	22.8	23.1	22.7
V_{OC} (V)	1.15	1.14	1.14	1.13	1.14	1.14	1.13	1.14
FF (%)	75.2	68.1	75.2	66.1	76.1	65.1	73.9	64.4
PCE (%)	20.15 ± 0.75	18.03 ± 1.02	20.35 ± 0.83	17.23 ± 0.89	20.16 ± 0.67	16.57 ± 0.98	19.62 ± 1.02	16.55 ± 1.02
HI	0.12		0.15		0.17		0.15	

10. Double-Halide Diffusion

to further confirm the coupling between D_V and D_{GB}, and specifically the inverse relationship between D_V and D_{GB}, we designed a double-halide diffusion experiment in which a mixed halide system $FA_{0.85}Cs_{0.15}Pb(I_{0.95}Cl_{0.05})_3$ (referred to as FACsICl) is brought in contact with the host $FAPbBr_3$. This experiment allows us to simultaneously monitor the diffusions of larger I^- and smaller Cl^- ions into $FAPbBr_3$. As can be seen in **Fig. S27**, Cl^- ions diffuse with a ~25 times faster diffusion rate into the volume of $FAPbBr_3$ compared to I^- ($D_V(Cl^-)= 4.3\times10^{-11}$ cm^2/s and $D_V(I^-)= 1.7\times10^{-12}$ cm^2/s). Meanwhile, Cl^- ions diffuse ~4 times slower along the GBs compared to their iodide counterparts ($D_{GB}(Cl^-)= 5.3\times10^{-9}$ cm^2/s and $D_{GB}(I^-)= 2.2\times10^{-8}$ cm^2/s). The faster diffusion of Cl^- into the volume of $FAPbBr_3$ can be attributed to the smaller ionic radius of Cl^- compared to I^-. This is consistent with prior observation that Cl in a small amount readily intercalates into an

iodide-bromide mixed halide perovskite phase, leading to a structural and optical change in these systems[25]. An interesting correlation appears when we consider the inverse D_{GB} *versus* D_V relation for Cl^- compared to I^- ions which follows the trend observed in cases of single ion diffusion into different MHPs. This inverse relationship further shows the close correlation between volume and GB diffusion properties of ions in MHPs. In summary, the GB strength model presented in our study consistently holds for a number of material compositions and passivation scenarios and shows that systems with a larger volume diffusion/smaller volume activation energy suffer from a small GB diffusion coefficient. This in turn explains why materials with significant aerobic photostability and will also result in devices with low *J-V* hysteresis and vice versa.

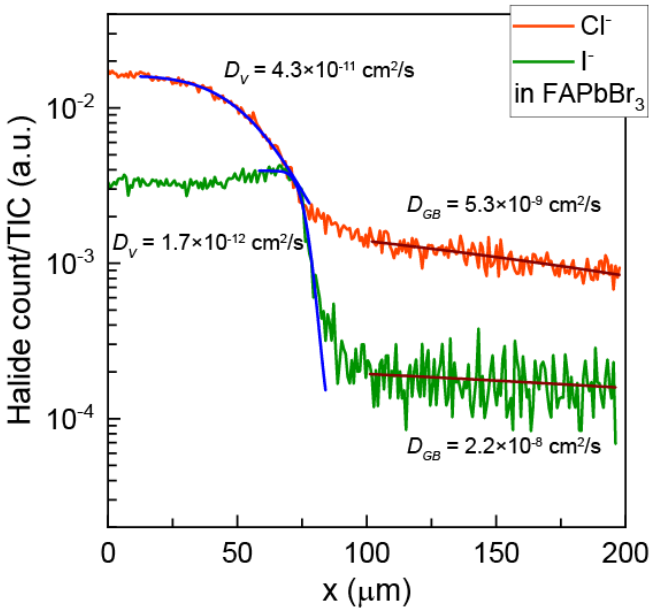

Fig. S27. Double halide 1D diffusion profile of Cl^- and I^- into the host $FAPbBr_3$ thin film. $FA_{0.85}Cs_{0.15}Pb(I_{0.95}Cl_{0.05})_3$ is used as the diffusion source for Cl^- and I^-. Samples were annealed at 100°C for 12 hours to form the diffusion front. The larger ion count of Cl^- compared to I^- is due to the larger electron affinity of chlorine.

11. GB passivation

We attribute the increase of D_{GB} and decrease of D_V in the cases of PEAI and PCBM passivation as successful examples of GB "strengthening" by promoting the confinement of fast moving ions in the GB channel. While further investigations are needed to shed light on how passivation agents strengthen GBs, it is reassuring to find analogs in other polycrystalline ceramics where an inverse relationship between volume and GB diffusions has been reported with doping, such as in the

diffusion of rubidium (Rb) into undoped and sodium (Na)-doped Cu(In,Ga)Se2, in which Na-doping led to a reduction of D_V but an increase in D_{GB}[8].

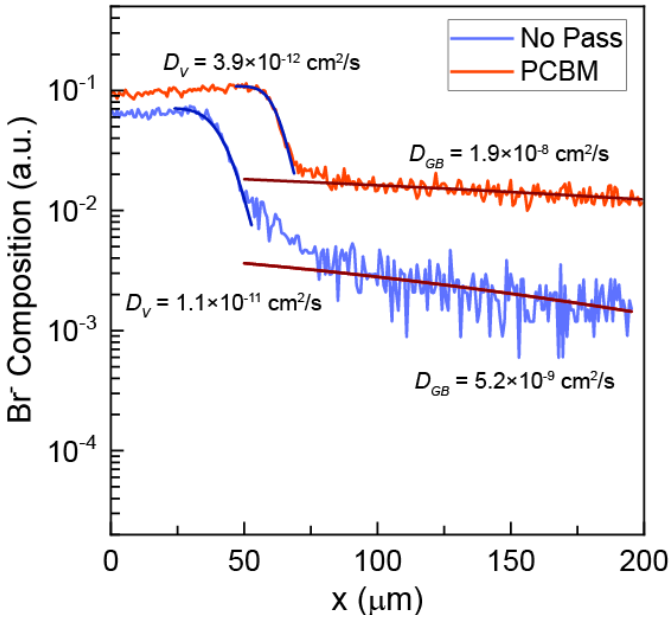

Fig. S28. 1D SIMS profiles of Br$^-$ diffusion into $MAPbI_3$ and PCBM passivated $MAPbI_3$ plotted against *x*. The blue and dark red solid lines show the volume and GB *erfc* fits for extraction of D_V and D_{GB}, respectively. The sandwiched samples were annealed for 6 hours at 100°C to form the diffusion edge. The diffusion values represented the average values extracted from two different diffusion profiles for each condition.

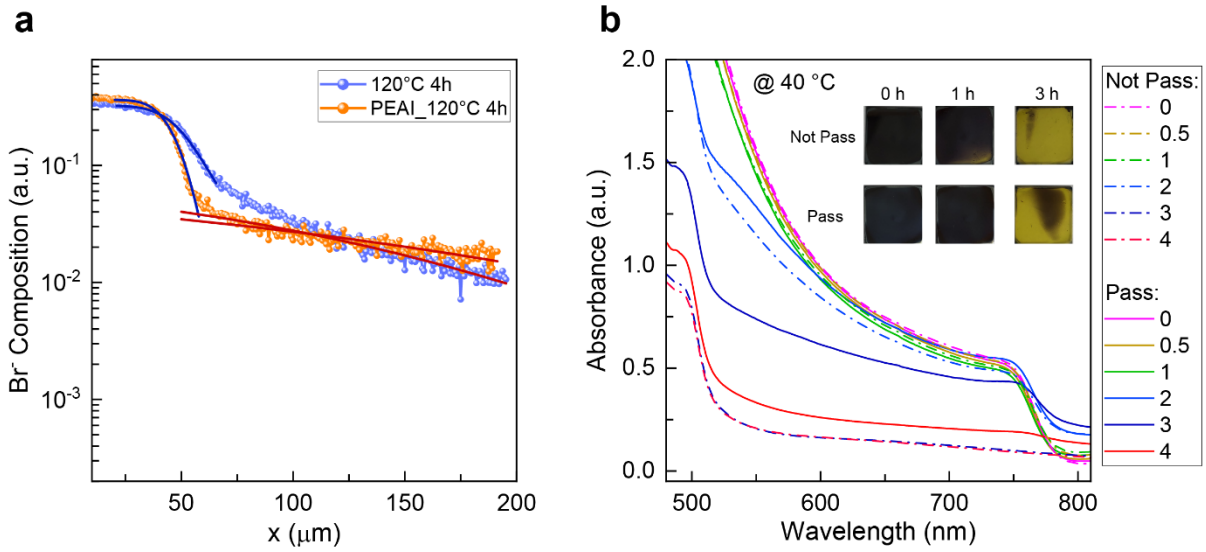

Fig. S29. **a**, 1D SIMS profiles of Br$^-$ diffusion into $MAPbI_3$ and PEAI passivated $MAPbI_3$ at 120°C plotted against *x*. The blue and dark red solid lines show the volume and GB *erfc* fits for extraction of D_V and D_{GB},

respectively. **b**, UV-Vis spectrum of as-prepared and passivated $MAPbI_3$ thin film exposed to 25 mW/cm^2 white light under a dry air environment in a Linkam stage at 40 °C.

12. Halide exchange

In lateral diffusion experiments, only the slope of the halide concentration profile is used for diffusion coefficient extraction. In exchange studies, on the other hand, the concentration of diffused ions is also important for tracking the bandgap change. For instance, in case of poor and sparse contact between the laminated MHP films, the reduced rate of diffusion of halides results in a slower rate of halide exchange and the rate of change of bandgap of both layers towards an equilibrium bandgap, referred to as homogenized state is impacted as well. Ensuring such experiments are used to extract the intrinsic diffusivity of halides, rather than an extrinsic diffusivity impacted by sample imperfections or lamination flaws, requires achieving intimate interfacial contact between the two MHP films. To do so, we have developed a hybrid lamination approach whereby one of the films, either $MAPbBr_3$ or $FAPbBr_3$, is coated on styrene ethylene butylene styrene (SEBS) block copolymer-coated glass, while the other is coated on glass. SEBS is a flexible polymer film that is removed from the glass substrate after MHP deposition and is laminated (face-down) onto the MHP-coated glass substrate. This allows the formation of sufficiently intimate contact between the MHP layers that will yield halide diffusion, exchange, and homogenization on timescales predicted based on the intrinsic diffusivity behavior measured for the volume diffusion coefficient of halides in our lateral diffusion study. For two layers with similar thicknesses, it has been shown that I^-/Br^- ratio reaches 50% in each layer[2]. The equilibrium bandgap is reached within 10 minutes in the case of hybrid lamination whereas rigid lamination does not allow equilibrium to be reached even after 24 hours (**Fig. S30**). **Fig. S31** shows SIMS depth profiles of Br^-, as a foreign ion, diffusing in the overlap region in the host FACsRbI. As can be seen, little to no gradient of foreign ions can be observed in the overlap region through the thickness of the host layer. The lack of such a gradient in the depth profile of Br^- ions diffused in FACsRbI points to a dominated diffusion mechanism that takes place laterally rather than a direct diffusion from the source, $FAPbBr_3$ film, which originally was in contact with FACsRbI at the top interface. Surprisingly, by increasing the annealing time, the foreign ion population in the host layer increases in a stepwise manner. Simply put, ions diffuse through the thickness of the grains and reach the opposite interface in a short amount of time when compared to homogenization time. This phenomenon shows that even ignoring the effects of fast ion diffusion through GBs, we

underestimate diffusion if we equate volume diffusion of ions with a combination of homogenization time and film thickness. The collective absorption spectra of bilayer samples before and after heat treatment at 120°C for different times are shown in **Fig. S32**. The continuous blue- and red- shifts in the starting iodide and bromide thin films, respectively, show the exchange of I^- and Br^- that changes the bandgap up to the point that I^-/Br^- ratio reaches an equilibrium composition (aka homogenization time).

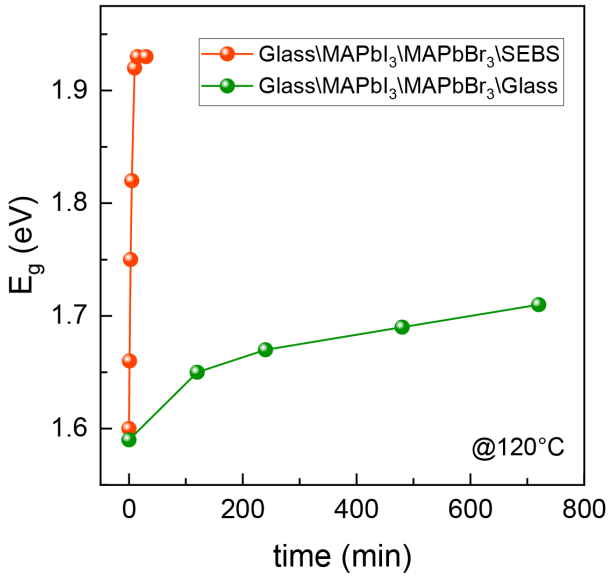

Fig. S30. **a**, bandgap change of laminated $MAPbI_3/MAPbBr_3$ with a rigid glass/glass and hybrid lamination samples glass/SEBS. As can be seen the homogenization bandgap in a hybrid lamination structure can be reached in around 10 minutes while the bandgap evolution continues behind 24 hours in the rigid lamination approach.

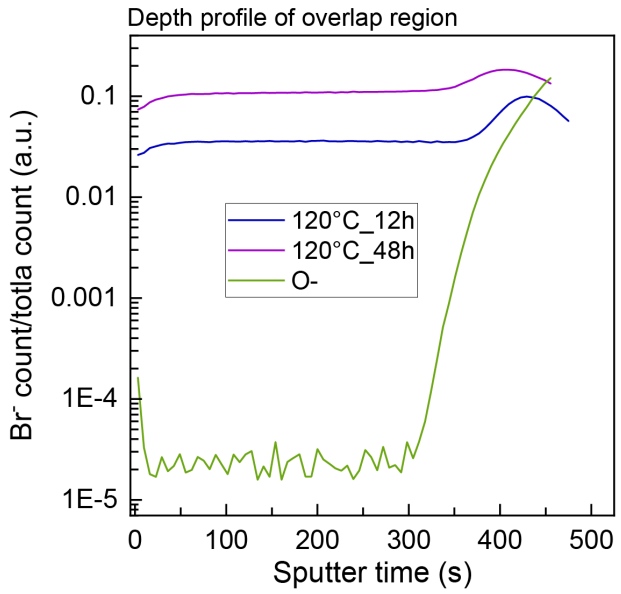

Fig. S31. Depth profile of Br^- signal through FACsRbI thin film after being in contact with $FAPbBr_3$ and baked at 120°C for 12 and 48 hours. The increase in the signal at around 400 s sputter time is related to the yield change due to the abundant presence of oxygen from the SiO_2 layer.

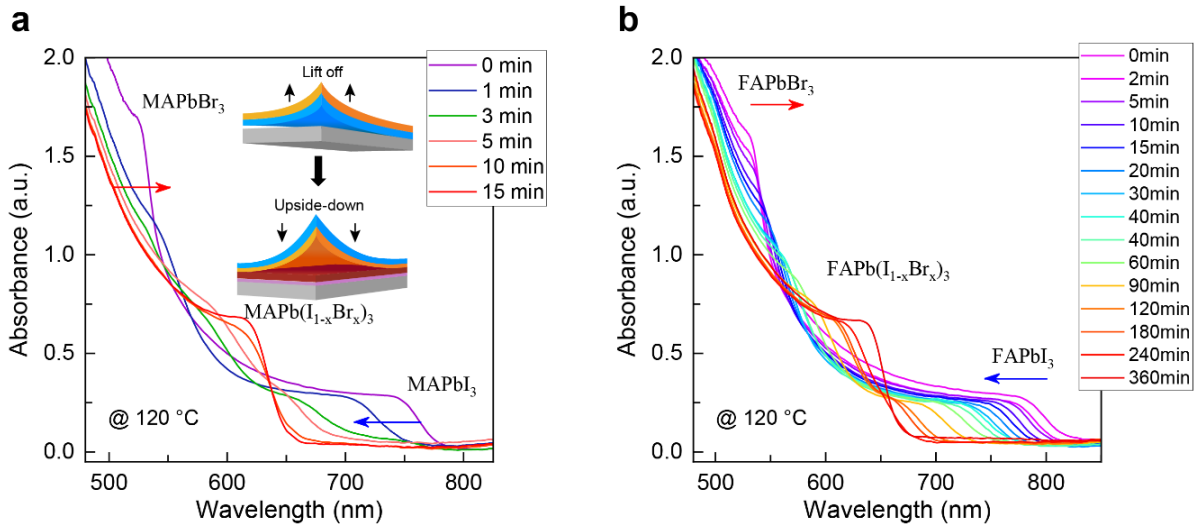

Fig. S32. UV-Vis absorption of bilayer **a**, $MAPbI_3/MAPbBr_3$ **b**, $FACsPbI/FAPbBr_3$ samples in a halide exchange study at 120°C. The inset in **a** shows the schematic of SEBS lamination to create a bilayer perovskite structure with intimate contacts.

References:

1. Heitjans, P. & Kärger, J. Diffusion in condensed matter: methods, materials, models. (Springer Science & Business Media, 2006).
2. Elmelund, T., Scheidt, R.A., Seger, B. & Kamat, P.V. Bidirectional Halide Ion Exchange in Paired Lead Halide Perovskite Films with Thermal Activation. *ACS Energy Lett.* **4**, 1961-1969 (2019).
3. Stephan, T., Flynn, G.J., Sandford, S.A. & Zolensky, M.E. TOF-SIMS analysis of cometary particles extracted from Stardust aerogel. *Meteoritics & Planetary Science* **43**, 285-298 (2008).
4. Richardson, G. et al. Can slow-moving ions explain hysteresis in the current–voltage curves of perovskite solar cells? *Energy Environ. Sci.* **9**, 1476-1485 (2016).
5. Mosconi, E. et al. Light-induced annihilation of Frenkel defects in organo-lead halide perovskites. *Energy & Environmental Science* **9**, 3180-3187 (2016).
6. Harrison, L. Influence of dislocations on diffusion kinetics in solids with particular reference to the alkali halides. *J. Chem. Soc. Faraday Trans.* **57**, 1191-1199 (1961).
7. Wuerz, R., Hempel, W. & Jackson, P. Diffusion of Rb in polycrystalline Cu(In,Ga)Se2 layers and effect of Rb on solar cell parameters of Cu(In,Ga)Se2 thin-film solar cells. *J. Appl. Phys.* **124**, 165305 (2018).
8. Laemmle, A. et al. Investigation of the diffusion behavior of sodium in Cu(In,Ga)Se2 layers. *J. Appl. Phys.* **115**, 154501 (2014).
9. Claire, A.D.L. The analysis of grain boundary diffusion measurements. *Br. J. Appl. Phys.* **14**, 351-356 (1963).
10. Fisher, J.C. Calculation of diffusion penetration curves for surface and grain boundary diffusion. *J. Appl. Phys.* **22**, 74-77 (1951).
11. Mehrer, H. Diffusion in solids: fundamentals, methods, materials, diffusion-controlled processes, Vol. 155. (Springer Science & Business Media, 2007).
12. Sajedi Alvar, M., Blom, P.W.M. & Wetzelaer, G.-J.A.H. Device Model for Methylammonium Lead Iodide Perovskite With Experimentally Validated Ion Dynamics. *Adv. Electron. Mater.* **6**, 1900935 (2020).
13. Sajedi Alvar, M., Blom, P.W.M. & Wetzelaer, G.-J.A.H. Space-charge-limited electron and hole currents in hybrid organic-inorganic perovskites. *Nat. Commun.* **11**, 4023 (2020).
14. Eames, C. et al. Ionic transport in hybrid lead iodide perovskite solar cells. *Nat. Commun.* **6**, 7497 (2015).
15. Bertoluzzi, L. et al. In Situ Measurement of Electric-Field Screening in Hysteresis-Free PTAA/FA0.83Cs0.17Pb(I0.83Br0.17)3/C60 Perovskite Solar Cells Gives an Ion Mobility of ∼3 × 10–7 cm2/(V s), 2 Orders of Magnitude Faster than Reported for Metal-Oxide-Contacted Perovskite Cells with Hysteresis. *J. Am. Chem. Soc.* **140**, 12775-12784 (2018).
16. Shao, Y. et al. Grain boundary dominated ion migration in polycrystalline organic–inorganic halide perovskite films. *Energy Environ. Sci.* **9**, 1752-1759 (2016).
17. Hoque, M.N.F., He, R., Warzywoda, J. & Fan, Z. Effects of Moisture-Based Grain Boundary Passivation on Cell Performance and Ionic Migration in Organic–Inorganic Halide Perovskite Solar Cells. *ACS Applied Materials & Interfaces* **10**, 30322-30329 (2018).
18. Phung, N. et al. The Role of Grain Boundaries on Ionic Defect Migration in Metal Halide Perovskites. *Adv. Energy Mater.* **10**, 1903735 (2020).
19. Liang, J. et al. Origins and influences of metallic lead in perovskite solar cells. *Joule* **6**, 816-833 (2022).

20. Ham, S. et al. Impact of Excess CH3NH3I on Free Carrier Dynamics in High-Performance Nonstoichiometric Perovskites. *J. Phys. Chem. C* **121**, 3143-3148 (2017).
21. Qiao, L., Fang, W.-H., Prezhdo, O.V. & Long, R. Suppressing Oxygen-Induced Deterioration of Metal Halide Perovskites by Alkaline Earth Metal Doping: A Quantum Dynamics Study. *J. Am. Chem. Soc.* **144**, 5543-5551 (2022).
22. Péan, E.V. et al. Investigating the Superoxide Formation and Stability in Mesoporous Carbon Perovskite Solar Cells with an Aminovaleric Acid Additive. *Adv. Funct. Mater.* **30**, 1909839 (2020).
23. Saidaminov, M.I. et al. Suppression of atomic vacancies via incorporation of isovalent small ions to increase the stability of halide perovskite solar cells in ambient air. *Nat. Energy* **3**, 648-654 (2018).
24. Habisreutinger, S.N., Noel, N.K. & Snaith, H.J. Hysteresis Index: A Figure without Merit for Quantifying Hysteresis in Perovskite Solar Cells. *ACS Energy Letters* **3**, 2472-2476 (2018).
25. Xu, J. et al. Triple-halide wide-band gap perovskites with suppressed phase segregation for efficient tandems. *Science* **367**, 1097-1104 (2020).